Review

Not peer-reviewed version

Chiral-Induced Spin Selectivity Effect for Advanced Battery Technologies and Electrochemical Energy Systems

Alberta Carella *, Francesco Rossella *, Claudio Fontanesi *

Posted Date: 1 April 2026

doi: 10.20944/preprints202603.2520.v1

Keywords: chiral-induced spin selectivity; chiral electrocatalysis; metal-air batteries; spin-dependent reaction pathways; energy conversion and storage

 doi:10.20944/preprints202603.2520.v1

Review

Chiral-Induced Spin Selectivity Effect for Advanced Battery Technologies and Electrochemical Energy Systems

Alberta Carella [1,*], Francesco Rossella [1,*] and Claudio Fontanesi [2,*]

[1] Department of Physics, Informatics and Mathematics (FIM), Univ. of Modena and Reggio Emilia, via Campi 213, 41125, Modena, Italy

[2] Department of Engineering "Enzo Ferrari" (DIEF), Univ. of Modena and Reggio Emilia, via Vivarelli 10, 41125, Modena, Italy

* Correspondence: alberta.carella@unimore.it (A.C.); francesco.rossella@unimore.it (F.R.); claudio.fontanesi@unimore.it (C.F.)

Abstract

The chiral-induced spin selectivity (CISS) effect enables spin-selective transport of electrons through chiral systems, linking handedness with spin polarization. This review provides a comprehensive examination of the emerging field of chiral electrocatalysis, detailing also the extensive experimental and theoretical endeavor conducted to gain a deeper understanding of the fundamental physical principles and mechanistic characteristics of this phenomenon. In particular, the CISS effect has garnered significant attention within the scientific community due to its potential for broad applicability across several fields, ranging from spintronics to biology**.** Among them, the prospective harnessing of CISS effect into electrocatalytic processes offers an innovative strategy to improve the performance of energy conversion and storage technologies. This review deeply examines the practical applications of the CISS effect across different electrocatalytic reactions, with particular emphasis on its influence on the oxygen reduction reaction (ORR) and its critical role in energy conversion systems where ORR reaction is a key process - such as in metal-air batteries, whose safety and performance can be enhanced through spin-selective electron transport.

Keywords: chiral-induced spin selectivity; chiral electrocatalysis; metal-air batteries; spin-dependent reaction pathways; energy conversion and storage

1. Introduction

About two decades ago, the revolutionary intuition of Professors Ron Naaman and David Waldeck about a possible correlation between chirality and electrons transport led to the discovery of the Chiral Induced Spin Selectivity (CISS) effect [4–6], term used to describe the phenomenon where electron transport through chiral systems leads to a spin polarization of the transmitted electrons. This means that when electrons move through a chiral system (e.g., helical molecules like DNA, peptides, or certain organic crystals) [7,8], there is a preference for one spin orientation (up or down), even in the absence of an external magnetic field or magnetic material. In common materials, electron spin — a fundamental physical property of electrons like charge — is randomly oriented and the two possible states (UP and DOWN, or +1/2 and −1/2). However, when an electron is transmitted through a chiral system, which lacks of inversion symmetry, one spin orientation is preferentially transmitted (Figure 1a) [9,10]. This leads to a spin-polarized current, even though the material itself is not magnetic. The discovery of this feature of chiral molecules subverts traditional knowledge that

 doi:10.20944/preprints202603.2520.v1

spin polarization requires magnetic fields or ferromagnetic materials, highlighting the role of molecular chirality in spin physics.

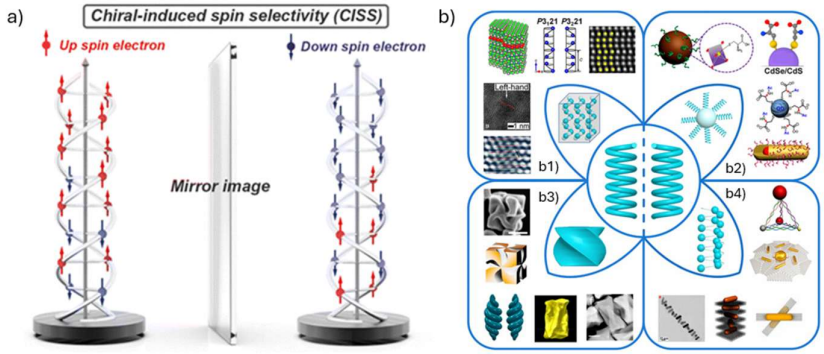

Figure 1. a) Schematic illustration of the CISS effect, depicting electron transfer through a chiral potential that promotes spin-selective transmission. Adapted from Ref. [11]. Reproduced by permission of The Royal Society of Chemistry. b) Schematic diagram of chirality origin in inorganic nanomaterials. Adapted with permission from Ref.[12]. Copyright 2023 American Chemical Society. More in detail, figure 1b reports (b1) Intrinsic chirality of chiral inorganic crystals. Adapted with permission from Ref.[13]. Copyright 2015 American Chemical Society. Adapted from Ref.[14] under terms of the CC-BY license. Adapted from Ref.[15]. Springer Nature. (b2) Chiral interactions between inorganic nanomaterials and chiral ligands. Adapted with permission from Ref.[16]. Copyright 2016 American Chemical Society. Adapted with permission from Ref.[17]. Copyright 2018, American Chemical Society. Adapted with permission from Ref.[18]. Copyright 2018 John Wiley and Sons. Adapted with permission from Ref.[19]. Copyright 2019 American Chemical Society. (b3) Chiral shapes at subwavelength scales. Adapted from Ref. [20]. Springer Nature. Adapted from Ref.[21]. Springer Nature. Adapted from Ref.[22] under terms of the CC-BY license. (b4) Chiral assemblies are formed by inorganic nanoparticles. Adapted with permission from Ref.[23]. Copyright 2012 American Chemical Society. Adapted with permission from Ref.[24]. Copyright 2015 American Chemical Society. Adapted from Ref.[25]. Springer Nature. Adapted with permission from Ref.[26] Copyright 2012 American Chemical Society.

Although initially controversial, the CISS effect is now widely accepted and is considered one of the most important discoveries in molecular electron transport. What makes Naaman and Waldeck discovery so significant is that it bridges the disciplines of physics, chemistry, and biology, offering a novel approach to manipulating electron spin. It provides a compelling explanation for previously unexplained spin-dependent phenomena observed in biological processes such as respiration (with reference to the oxygen reduction and evolution reactions, ORR and OER, respectively) and photosynthesis. Building on these biological insights, researchers have increasingly turned their attention to systems - particularly chiral inorganic nanomaterials - where chirality can be precisely engineered in the laboratory [8,12]. Inorganic material synthesis typically enables a higher degree of precision in tuning both crystal architecture and chiral properties, which can significantly improve their efficiency and functional capabilities, offering a promising platform to harness the CISS effect in a controlled manner. A more in-depth illustration of spin-polarization observations in chiral inorganic nanomaterials is provided in Figure 1b. The discovery of CISS effect demonstrated that chiral systems can selectively transmit electrons with one spin over those the opposite spin, paving the way of exploiting chiral inorganic/organic architectures as spin filter and [27–31] opening new avenues for spin-selective transport to be used in practical applications, ranging from green energy technologies, catalysis to quantum computing, highlighting its broad scientific and technological impact.[32]

In the following sections, we first review key measurement techniques and experimental evidence and that have validated spin-selective transport in chiral systems. Building on these foundations, we examine the potential of CISS-active materials for applications in energy conversion

 doi:10.20944/preprints202603.2520.v1

and storage technologies, with a particular focus on metal–air batteries. Finally, we outline future research directions aimed at integrating CISS principles into the design of next-generation electrochemical systems, emphasizing the need for deeper mechanistic understanding and scalable material strategies.

2. Experimental Demonstration of CISS Effect

Although numerous theoretical studies have offered convincing explanations of the CISS effect, experimental evidences remain essential for its validation.

2.1. Photoemission Experiments

The first experimental evidence for CISS came from low-energy photoelectron transmission (LEPET) spectroscopy using Langmuir–Blodgett films of amino acids deposited on a gold substrate[4,33] (Figure 2a). Subsequent investigations applying the same technique have validated these results on a wide range of chiral molecular layers [34–38]. In this setup, CPL was used to excite spin-polarized photoelectrons in gold (Au), and the resulting photoelectron yield was measured in relation to the chirality of the amino acid films. The experiment showed a clear correlation between the photoelectron yield and the combination of CPL polarization and molecular chirality. However, since the spin of the transmitted photoelectrons was not directly measured, the evidence for spin polarization was only indirect.

A more definitive demonstration came later from Göhler et al.[39–41], who used a Mott detector to directly measure the spin polarization of photoelectrons (Figure 2b). They found that spin polarization from the bare gold surface depended on the polarization of the CPL, consistent with previous results using Langmuir–Blodgett films. More specifically, the spin polarization of photoelectrons emitted from the bare Au (111) surface was modulated by the polarization state of the incident light, varying from −22% under right-handed circularly polarized light to 0% with linearly polarized light, and up to +22% with left-handed circularly polarized light (Figure 2c) [5]. However, when a self-assembled monolayer (SAM) of double-stranded DNA was applied to the surface, this dependence on light polarization was markedly reduced, with spin polarization values confined to a narrower range of −35% to −29% (Figure 2d,e,f) [5]. These findings indicate that DNA molecules function as spin-selective filters. Notably, the degree of spin polarization was shown to increase monotonically with the length of the DNA duplex, reaching approximately 60% for SAMs composed of 78-base pair duplexes [5]. This evidence, i.e. the fact that the degree of spin polarization could be tuned by adjusting the length of the DNA duplex, supported the conclusion that the observed spin-selective behavior, characteristic of the CISS effect, originates from the intrinsic chiral properties of the DNA molecules rather than from the gold–SAM interface.

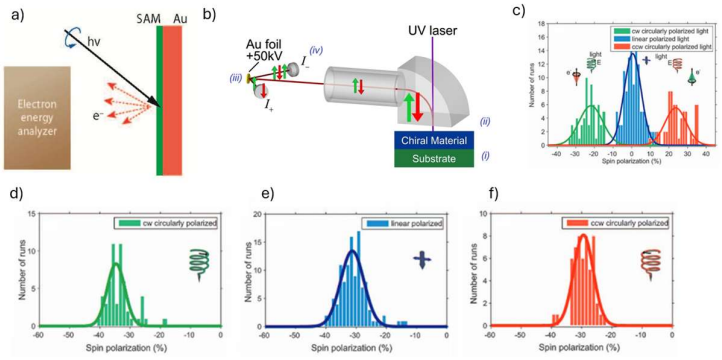

Figure 2. a) Schematic of the LEPET photoemission setup used to measure electron energy distributions transmitted through chiral monolayers, without spin resolution of the emitted electrons. Adapted with permission from Ref.[5]. Copyright 2012 American Chemical Society. b) A representative schematic diagram illustrates the determination of CISS via Mott polarimetry measurements. Initially, (i) photoelectrons are excited

 doi:10.20944/preprints202603.2520.v1

within the substrate, (ii) then pass through a chiral spin filter, which induces a net spin polarization. These photoelectrons are subsequently (iii) scattered by a gold foil target based on their spin orientation, and (iv) the resulting signals are measured by two independent detectors. c) Measured spin-polarized electron distributions for photoemission from bare Au under illumination with right-handed circularly polarized light (green), left-handed circularly polarized light (red), and linearly polarized light (blue). The corresponding mean longitudinal spin polarizations are −22%, +22%, and 0%, respectively. Adapted from Ref.[6] under terms of the CC-BY license. d-f) Spin polarization of photoelectrons emitted from an Au(111) surface coated with double-stranded DNA, under clockwise, linear, and counterclockwise excitation, respectively. Adapted from Ref.[6] under terms of the CC-BY license.

In photoemission experiments, the spin filtering effect can be assessed as high-energy photoelectrons travel through the chiral organic layer toward the detector. Thus, analyzing the energy of emitted electrons provides further means of verifying CISS.

2.2. Magneto-Conductive Atomic Force Microscopy (mc-AFM)

This spin-dependent behavior is further supported by transport measurements conducted using conductive atomic force microscopy (mc-AFM) [42–44]. In a typical study based on this method[42], the conductance of a gold nanoparticle-dsDNA-nickel molecular junction was recorded while varying the magnetization direction of the ferromagnetic (FM) nickel substrate (Figure 3a). By changing the direction of the substrate's magnetization, it was possible to break the degeneracy of nickel's valence electron spin states, favoring alignment of one spin direction with the field. A straightforward analysis of the average I–V curves recorded (Figure 3b-d) reveals that the conductance of the DNA-based molecular junction depends on the direction of the magnetic field.

When electrons are emitted from magnetized nickel (Ni), they mostly are majority electrons, coming from the more stable energy subbands. If their spin matches the preferred spin direction for transport through the chiral molecule, the current for this direction of the magnetic field will be higher than that measured when the Ni magnetization is in the opposite direction and the electrons have the opposite spin orientation, which is unfavored by the helicity of the chiral molecule. When the direction of electron flow is reversed (i.e., negative current), the preferred spin is that aligned in the other direction. In this case, the spin orientation favored for transmission aligns with the minority electron sub-band in Ni, which features a high density of states above the Fermi level, thus facilitating electron injection into the Ni and enhancing current flow (Figure 3e).

In sum, the I–V (current–voltage) curves resulted from mc-AFM measurements, disclosing changes in molecular conductance depending on the magnetic field direction, confirmed a spin-selective transport in the tunneling regime which is consistent with the CISS effect.

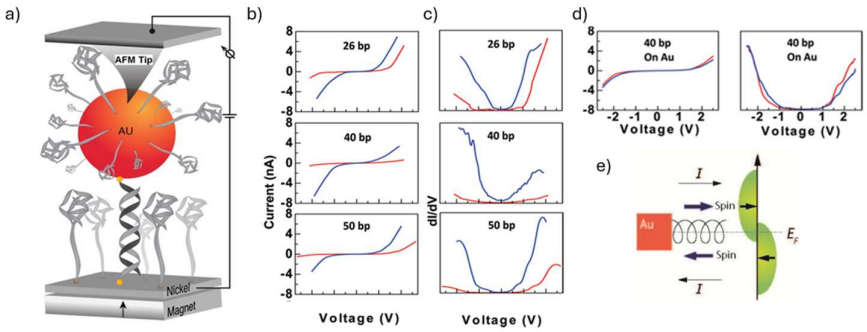

Figure 3. a) The mc-AFM setup used to measure the conductance of a nanoparticle–dsDNA–nickel molecular junction: A self-assembled monolayer (SAM) of single-stranded DNA (ssDNA) is adsorbed onto the nickel substrate. When complementary ssDNA strands are attached to gold nanoparticles, hybridization occurs, forming a nanoparticle–double-stranded DNA–nickel complex. As a result, the dsDNA oligomers are anchored

 doi:10.20944/preprints202603.2520.v1

at one end to the nickel surface (serving as the bottom electrode) and at the other end to the gold nanoparticles (top electrode) via chemical bonds. A permanent magnet placed beneath the nickel substrate orients its magnetic field with either the north or south pole facing the substrate, corresponding to "up" and "down" magnetization configurations, respectively. The electrical current is measured between the nickel substrate and the AFM tip in contact with the gold nanoparticle. b) The average current obtained for the three oligomers studied when the magnetic field is pointing up (red) or down (blue). c) The density of states (dI/dV) obtained for the three oligomers based on the averaged current for the magnetic field pointing up (red) or down (blue). d) For control, the bottom panel shows the signal obtained with a gold substrate when no specific spin is injected. Adapted with permission from Ref.[42]. Copyright 2011 American Chemical Society. e) A diagram showing the density of states in magnetized nickel. Electrons flowing out of the nickel mostly have majority spin, while electrons coming from the gold nanoparticle must have minority spin to enter the nickel. Adapted with permission from Ref.[5]. Copyright 2012 American Chemical Society.

Though mc-AFM is a valuable tool for demonstrating the existence of the CISS effect, as it allows for the measurement of current through chiral molecules and can reveal asymmetries in transport that suggest spin-dependent behavior, alone it is not sufficient to definitively measure the effect, as it does not provide direct information about electron spin polarization. So, while such results may provide indirect evidence for the presence of CISS, to truly measure the spin selectivity that defines this effect, magnetic conductive AFM (mc-AFM) is required. In mc-AFM, either the AFM tip or the substrate is magnetized, introducing a well-defined spin polarization into the system. By applying a magnetic field to reverse the magnetization and observing corresponding changes in the measured current, one can detect a spin-dependent transport signal[45–47]. This modulation of current with magnetic reversal is a direct signature of the CISS effect and cannot be captured by c-AFM alone.

2.3. Electrochemical Observations

Cyclic voltammetry (CV) can provide insightful evidence for the CISS effect by revealing spin-dependent electron transfer processes at chiral interfaces. In a typical CV experiment involving a chiral molecule immobilized on an electrode, the electrochemical response - such as peak current or peak potential - can differ depending on the spin polarization of the electrons involved in the redox process. [48,49]

A recent study[50] has demonstrated that electrochemical measurements on a chiral tetrathiafulvalene (cTTF) derivative - part of a well-studied class of molecules known to exhibit the CISS effect [51] - enable effective characterization of enantio-recognition involving bulk interactions. This finding aligns with earlier reports on bulk-mediated enantio-recognition, where cyclic voltammetry revealed chiral discrimination in systems using chiral ionic liquids as solvents for chiral redox couples [52–54]. The CV pattern of enantiopure solutions of cTTF is significantly modified in the presence of enantiopure tartaric acid, indicating an interaction between the chiral species (Figure 4a-d). These electrochemical measurements serve as effective tools for monitoring the chiral recognition process, specifically in distinguishing between symmetric and dissymmetric enantiomeric intermolecular interactions. As proposed in recent publications[55–58], spin-driven interactions may play a role in mediating these intermolecular chiral recognition phenomena.

This points toward a mechanistic connection with the CISS effect, in which electron transmission through chiral molecules is accompanied by spin polarization. Theoretical models suggest that spin-dependent interactions [55–58] - such as those invoked in the CISS effect - may play a pivotal role in driving enantioselectivity. In the CISS framework, electron transport through chiral systems is inherently spin-selective due to spin–orbit coupling and the chiral potential landscape, even in the absence of magnetic electrodes. It has been proposed that similar spin-dependent forces could influence the energetics of intermolecular interactions, such as those involved in chiral recognition, by favoring spin-compatible configurations between interacting chiral partners. This implies that the underlying physics of CISS might extend beyond solid-state charge transport and influence

 doi:10.20944/preprints202603.2520.v1

supramolecular recognition in solution-phase systems, even when no direct spin polarization is measured.

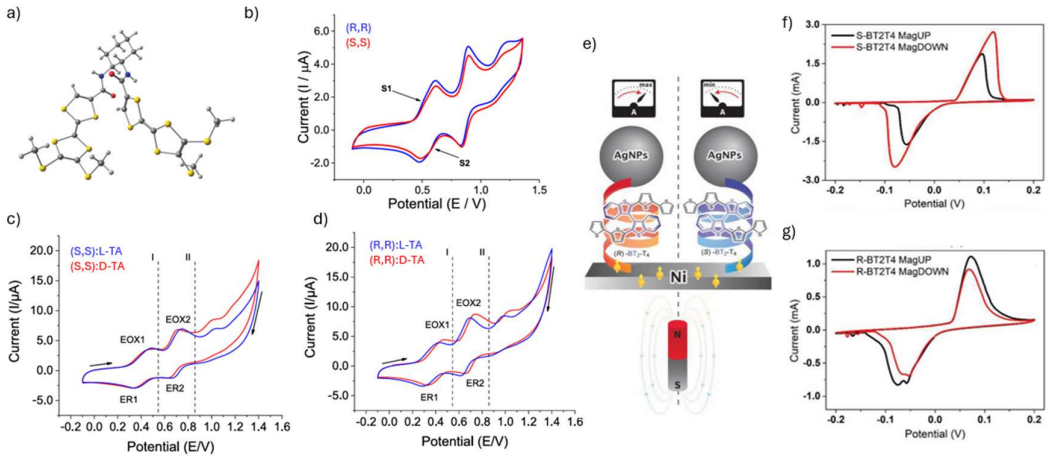

Figure 4. a) Ball and stick representation of the molecular structure of an enantiopure TTF chiral derivative, i.e (S,S) bis (tetrathiafulvalene)-1,2-cyclohexane-diamine. Color code used for the atoms are yellow for sulphur, turquoise for nitrogen, red for oxygen, grey for carbon and white for hydrogen. b) CV curves of 5 mM enantiopure solutions of (R,R) and (S,S) derivative, represented with blue and red curve respectively; CV curves of 5 mM enantiopure solutions of c) (S,S) and d) (R,R) enantiomer in the presence of enantiopure tartaric acid (L- or D- TA) (0.5 mM), using 0.1 M TBATFB in ACN as base electrolyte. GC, Ag/AgCl/KCl, and Pt are the WE, RE, and CE, respectively. 0.1 M TBATFB in ACN is the base electrolyte, and 50 mV s^{-1} is the potential scan rate. (a-d) Adapted from Ref.[50]. © Wiley 2024. e) Schematic representation of spin-dependent CV setup. f) spin-dependent cyclic voltammetry obtained with a magUP (black line) and MagDOWN (red line) for f) S and g) R chiral TTF derivative. (e-g) Adapted from Ref.[59]. © Wiley 2024.

Building on these findings, spin-dependent electrochemical (SDE) techniques offer a complementary approach for directly probing the role of spin polarization in chiral redox processes. When a magnetized electrode is used, reversing the direction of magnetization can lead to measurable changes in the voltammogram, such as shifts in oxidation or reduction peaks or variations in current intensity. These changes arise from the spin-selective interaction between the chiral molecules and the spin-polarized electrons provided by the magnetized electrode[60] .

Indeed, a 2024 study demonstrated that the I–V curves obtained from SDE measurements using TTF-derivative-based electrode exhibit clear spin-injection dependence, where the efficiency of charge transmission depends on the handedness of the chiral interface [59] (Figure 4e-g). This behavior suggests that the differences in current observed - driven by chiral recognition - can be understood within the framework of the chiral-induced spin selectivity effect. Specifically, in the case of the above-mentioned study, when a chiral layer with S-handedness preferentially conducts spin-up electrons, high conduction is observed if the adjacent facing layer also has S-handedness (a symmetric interface). Conversely, if the facing layer has R-handedness (an asymmetric interface), the conduction is reduced. Reversing the handedness of both layers produces the mirror-opposite scenario. These findings point to spin as a hidden driving force in chiral recognition.

In other words, chiral-modified electrodes (e.g., with chiral TTF derivatives) exhibit significant spin-filtering during SDE measurements, acting as direct manifestations of the CISS effect in bulk electrochemistry. This supports the notion that spin-polarized electron transfer in redox processes can be influenced by molecular chirality, providing a mechanistic bridge between enantioselective recognition and CISS-driven spin-filtering phenomena. Since the CISS effect predicts that electron transport through chiral molecules is spin-dependent, the magnetization-dependent electrochemical response observed in CVs can serve as strong evidence of spin selectivity. Importantly, this approach combines the sensitivity of electrochemical techniques with the ability to probe spin-dependent

 doi:10.20944/preprints202603.2520.v1

processes, offering a relatively accessible and scalable method to investigate CISS in a variety of chiral molecular systems.

The following Section 2.3 provides an overview of the principal experimental methodologies utilized for the quantitative measurement of the CISS effect, mc-AFM technique included.

2.4. CISS Effect Detection

2.4.1. mc-AFM

The mc-AFM technique probes spin selectivity in nanoscale structures, considering the influence of the interface between chiral materials and the ferromagnetic electrode used for spin analysis.

Unlike standard single-molecule measurements, which often require precise molecular junctions between chiral molecules and FM substrates (a technically demanding process), mc-AFM simplifies the setup. It requires only that the conductive AFM tip, coated with FM material, be pre-magnetized using a permanent magnet (Figure 5a) [61,62]. When tips magnetized in different directions were used, the recorded I–V curves exhibited asymmetric behavior depending on the handedness of the chiral molecule and the direction of magnetization, providing further evidence of the CISS effect. In line with the preceding discussion on TTF-based chiral systems, this approach is here exemplified by the enantiopure derivative TM-BEDT-TTF, whose molecular structure, crystal morphology, and mc-AFM characterization are shown in Figure 5b-c-d.

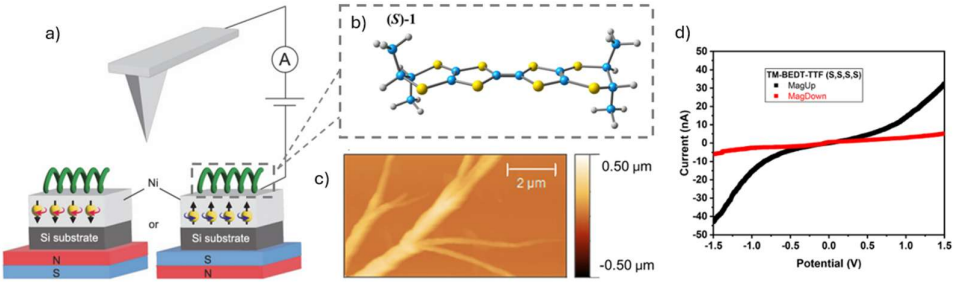

Figure 5. a) Schematic of the mc-AFM set-up used to detect CISS. The ferromagnetic substrate injecting spin-polarized electrons in the monolayer of chiral molecules is magnetized up or down with an external magnet. Adapted from Ref.[63] under terms of the CC-BY license. b) Ball and stick representation of the molecular structure of an enantiopure tetrathiafulvalene (TTF) chiral derivative, i.e. tetramethyl-bis(ethylenedithio)-tetrathiafulva lene (TM-BEDT-TTF), an extensively studied class of chiral inducers at the nanoscale. color code used for the atoms are yellow for sulphur, turquoise for carbon and grey for hydrogen. c) AFM images of the crystal morphology and d) mc-AFM of TM-BEDT-TTF. mc-AFM experimental I–V curves are recorded in the −1.5 V to +1.5 V potential range and detected a spin polarization value in the 30% to 50% range. (b-d) Adapted from Ref.[51]. Reproduced by permission of the Royal Society of Chemistry.

The current–voltage curves observed in mc-AFM measurements can be interpreted using a model in which the applied voltage induces charge polarization in the chiral system, which in turn leads to spin polarization[58,64]. In this model, a chiral molecular film is situated between two electrodes, one of which is ferromagnetic. The applied electric field polarizes the chiral molecules, and due to the chiral nature of the system, this charge polarization is accompanied by spin polarization in an enantiospecific manner, i.e., the association between charge polarity and spin orientation depends on the handedness of the chiral molecules. Consequently, electrons injected from the ferromagnetic electrode encounter a spin-dependent potential barrier. The height of this barrier is proportional to the product of the localized charge at the molecular pole and the spin-exchange interaction. Assuming a charge polarization of approximately 10% of an elementary charge and a spin-exchange interaction energy on the order of 1 eV, the resulting spin-dependent difference in barrier height is estimated to be ~100 meV [6]. Experimental findings support this estimate, as they reveal a similar magnitude in the difference between injection barriers for opposite spin states[42].

 doi:10.20944/preprints202603.2520.v1

This spin-dependent barrier provides a plausible explanation for the high spin selectivity observed at room temperature. Other studies have proposed 'spinterface' models [65–67] to provide a more quantitative explanation of these experimental observations, justified by the evidence that the first CISS experiments were performed with supramolecular assemblies of chiral molecules on metal electrodes. However, despite their intrinsic limitations, more simplified models have proven effective in providing valuable insights into the CISS effect and the properties of chiral molecules associated with it.

Spin polarization in mc-AFM measurements is typically quantified either as the ratio of currents obtained with opposite magnetization orientations at a given voltage, SP = $(I_{\uparrow}/I_{\downarrow})_V$, or as the spin polarization percentage, calculated as: $SP_{\%} = \left[\frac{I_{\uparrow} - I_{\downarrow}}{I_{\uparrow} + I_{\downarrow}}\right] x\ 100$. Because mc-AFM operates in a nonlinear conduction regime, it is highly sensitive to subtle changes in spin polarization, making it an effective tool for quantifying spin-selective transport phenomena. Furthermore, its setup and the local nature of the measurement allow for efficient screening of spin-selective transport in a wide range of materials, including disordered or self-assembled films, enabling the characterization of heterogeneous or structurally complex systems, which is essential for correlating molecular chirality, interface effects, and spin-dependent conduction on the nanoscale.

So, to date, mc-AFM is considered one of the most suitable techniques to investigate the CISS effect, allowing the direct measurement of spin-dependent currents when electrons as electrons are injected into or extracted from chiral molecular layers under controlled bias.

2.4.2. Circular Dichroism (CD)

Circular dichroism and the CISS effect are fundamentally linked through the electronic properties of chiral systems [56,68]. CD reflects a molecule's differential interaction with left- and right-circularly polarized light, arising from asymmetries in its electronic transitions due to chirality. Similarly, the CISS effect reveals that electron transmission through chiral molecules becomes spin-polarized, a phenomenon rooted in spin–orbit coupling and the helical potential landscape experienced by moving electrons. Recent theoretical and experimental studies suggest a strong correlation between a molecule's CD spectrum and its ability to induce spin polarization, indicating that both phenomena originate from the same chiral electronic structure. In this view, CD can be seen as the optical analogue of spin selectivity, and the magnitude of the CISS effect may reflect the degree of electronic asymmetry responsible for optical activity. This correlation underscores a deeper, intrinsic connection between chiro-optical responses and spin-dependent charge transport, revealing that chiral matter encodes its handedness not only in how it interacts with light, but also in how it controls the spin of electrons.

For instance, recent work by Mujica and Fay employs an "electron on a helix" model to investigate the interplay between circular dichroism and the CISS effect [69,70]. In these studies, a rationale is proposed for the correlation between the spin-polarized electronic response and the circular dichroism associated with helical systems, pointing to a fundamental link between CISS-related phenomena and chiro-optical properties, both governed by the electronic structure of chiral systems.

2.4.3. Optical Rotation in Photoluminescence Experiments

Given that spin selectivity can affect the optical properties of materials, it is also expected to influence their photoluminescence (PL) behavior. Notably, the CISS effect has been shown to enable polarized emission at the single-photon level, highlighting its role in spin-dependent optical phenomena and giving rise to what can be described as a CISS-induced optical rotation effect [51,71,72].

In PL experiments, a sample is typically excited with light, and the resulting emission is analyzed. When the CISS effect is active, it can induce optical rotation in the PL signal, even in the absence of an external magnetic field[73,74], as the helical motion of electrons generates effective

 doi:10.20944/preprints202603.2520.v1

magnetic fields that couple molecular handedness to spin-polarized emission, including circularly polarized photoluminescence (*CPL*) from quantum emitters on chiral substrates (Figure 6a-c).

More specifically: upon illumination with unpolarized or linearly polarized light, a chiral molecule - or a system interfaced with a chiral structure - can exhibit spin-selective excitation due to the CISS effect, which preferentially promotes electrons of a specific spin orientation. This spin-selective process leads to an asymmetric population of spin-polarized excited states, wherein the chiral environment further stabilizes or modulates spin-dependent relaxation pathways. The subsequent recombination of these spin-polarized carriers gives rise to *CPL*. The emitted photoluminescence thus exhibits a net optical rotation, observable either as a difference in emission intensity between left- and right-circularly polarized components ($\Delta I = I_{LCP} - I_{RCP}$) or as a rotation in the polarization plane of the emitted light (Figure 6d-e).

The degree of polarization in the PL signal, often characterized by the circular polarization parameter $P_C = \frac{I_{LCP}-I_{RCP}}{I_{LCP}+I_{RCP}}$ reflects the extent of spin polarization induced by the CISS effect. This optically active emission arises not solely from the intrinsic chiroptical properties of the molecule but rather emerges from and is amplified by the non-equilibrium spin distribution generated during the excitation process by the CISS effect.

Such CISS-induced optical rotation in PL is particularly enhanced in systems comprising chiral molecular layers in combination with materials exhibiting strong spin–orbit coupling or ferromagnetic interfaces, where spin injection and detection are more efficient. These observations underscore the role of spin–chirality interactions in modulating light emission, providing a powerful optical probe for spin-selective processes in chiral systems.

It is worth noting that the enhanced *CPL* detection enabled by CISS-mediated spin-polarized transport not only serves as compelling evidence for the existence of the CISS effect, but also represents a powerful tool with potential applications across diverse fields, including quantum optics [75,76], electronic[77] and communication technologies [78] .

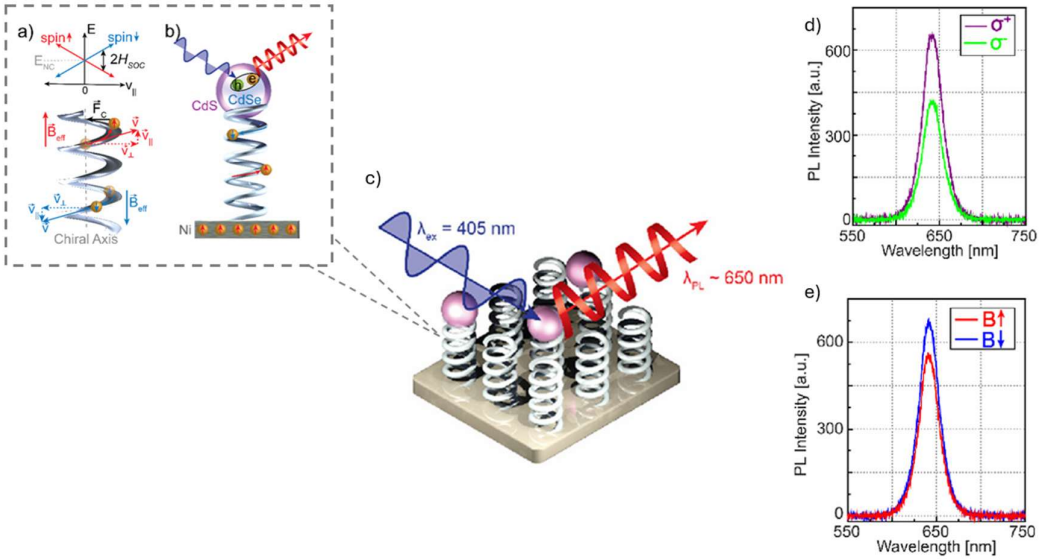

Figure 6. a) Schematic representation of the forces and effective magnetic fields induced by chirality associated with electron motion along a right-handed helix. Electrons moving upward ($v_{||} > 0$) are represented by red arrows, while those with downward trajectories ($v_{||} < 0$) are indicated by blue arrows, illustrating the directional dependence of chiral-induced interaction. b) Model diagram illustrating circularly polarized photoluminescence emitted from a single quantum light emitter anchored to an out-of-plane magnetized Ni surface via a right-handed chiral molecule. c) Schematic representation of the excitation process in CdSe/CdS quantum dots (QDs) deposited on a chiral substrate. d) PL spectra of a single 9 ML QD measured under into-plane surface magnetization, revealing a dominant right-handed (purple) circular polarization. e) Total PL intensity recorded

 doi:10.20944/preprints202603.2520.v1

from the same QD under opposite magnetization directions: into the surface plane (blue) and out of the surface plane (red). (a-e) Adapted with permission from Ref.[71]. Copyright 2024 American Chemical Society.

3. Application of CISS Effect in the Energetic Field: The Case of Meta-Air Batteries

3.1. Overview

The CISS effect has recently garnered significant attention for its potential to enhance the efficiency of various energy conversion and storage technologies through spin-selective processes (Table 1).

In photovoltaic systems, for example, chiral hybrid organic–inorganic perovskite structures were able to induce spin polarization in photo-generated charge carriers, thereby enhancing the power conversion efficiency of organic and hybrid solar cells. This spin polarization effectively suppresses electron-hole recombination, leading to improved charge separation and extended carrier lifetimes. Notably, devices incorporating chiral perovskites or chiral organic interlayers have demonstrated performance enhancements of up to two- to four-fold due to the CISS effect. [8,79–81]. In particular, a two-dimensional layered perovskite thin films incorporating R-/S-methylbenzylammonium (MBA) have demonstrated spin polarizations as high as 92%, resulting in enhanced power conversion efficiencies. [82] (Figure 7a).

Spintronics, which leverages the spin degree of freedom of electrons, stands to benefit from the CISS effect by enabling spin polarization without the need for external magnetic fields or heavy metals[83]. This advancement paves the way for the development of lightweight, low-power spin-based devices, which are particularly attractive for applications in energy-efficient computing systems and the Internet of Things (IoT)[29,84–86].

Table 1. Summary of the main energy-related application areas for exploiting the CISS effect and its associated benefits.

Application Area	CISS Benefit	Energy Impact
Solar cells	Spin-polarized charge separation	Higher efficiency
Fuel cells/electrolyzers	Spin-selective catalysis	Lower overpotential, better selectivity
Spintronics	Low-power spin devices	Energy-efficient electronics
Thermoelectrics	Modified spin transport	Improved thermoelectric performance
Artificial photosynthesis	Spin-controlled electron flow	More efficient solar fuel generation

Thermoelectric materials, which convert temperature gradients into electrical voltage, can also be enhanced through the CISS effect. By influencing spin-dependent charge transport, the CISS effect has the potential to improve the Seebeck coefficient and reduce thermal conductivity, thereby increasing the thermoelectric figure of merit (ZT). While research in this area is still emerging, initial studies suggest promising avenues for the integration of chiral molecules into thermoelectric systems[87].

Artificial photosynthesis systems (Figure 7b), which aim to mimic natural photosynthetic processes for solar fuel generation, may benefit from the CISS effect. The spin-selective transport of electrons facilitated by chiral components can enhance the efficiency of solar-to-chemical energy conversion[88]. For example, chiral ZnO photocatalysts have demonstrated improved performance in water-splitting reactions [89], attributed to the alignment of unpaired electron spins in hydroxyl radicals, thereby favouring the formation of triplet oxygen over undesired byproducts (Figure 7c).

 doi:10.20944/preprints202603.2520.v1

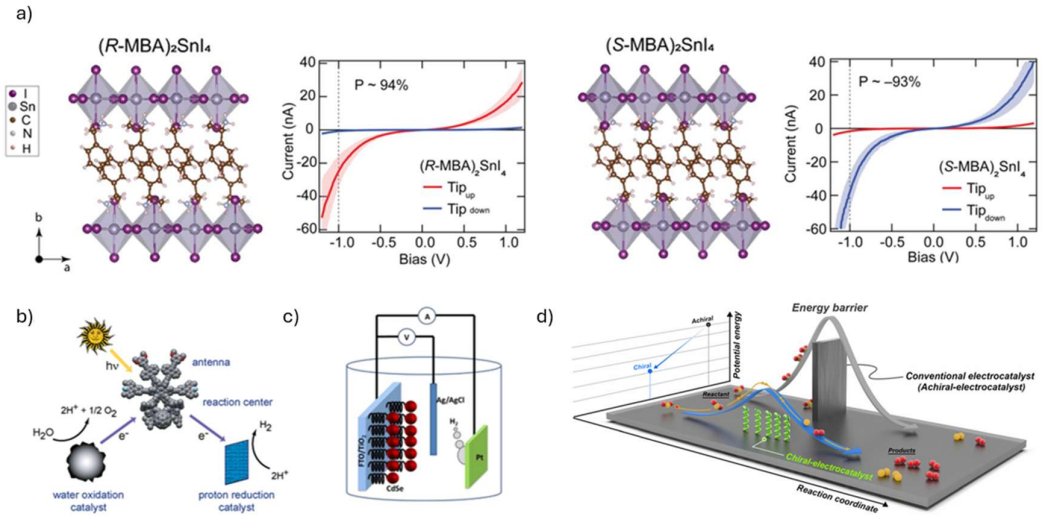

Figure 7. a) Side-view crystal structures along the *c*-axis of (R-MBA)$_2$SnI$_4$ and (S-MBA)$_2$SnI$_4$ chiral 2D hybrid structured and related room-temperature mc-AFM I-V curves recorded on 50-60 nm thick films. Adapted with permission from Ref.[82]. Copyright 2020 American Chemical Society. b) Key reactions involved in artificial photosynthesis. Adapted with permission from Ref.[88]. Copyright 2009 American Chemical Society. c) Artificial photosynthetic water splitting cell, in which light is used to generate hydrogen. Adapted with permission from Ref.[89]. Copyright 2015 American Chemical Society d) Schematic illustration of the activation energy barrier in chiral versus achiral electrocatalysts, highlighting the CISS effect. Adapted from Ref.[11]. Reproduced by permission of the Royal Society of Chemistry.

Lastly and most notably in the context of this review, in the realm of electrocatalysis (Figure 7d), particularly concerning the oxygen evolution reaction (OER) and oxygen reduction reaction (ORR), the CISS effect plays a pivotal role [90,91]. The OER involves the formation of triplet oxygen (O_2), and spin alignment facilitated by chiral catalysts can lower the reaction overpotential and suppress the formation of undesired byproducts such as hydrogen peroxide. [92–94]. For instance, chiral iron oxide nanoparticles have exhibited up to an 89% improvement in current density at 1.8 V versus the reversible hydrogen electrode (RHE), attributed to the synergistic impact of inherent magnetic moments and chirality[92]. Substantial enhancements arising from the CISS effect have likewise been observed in the oxygen reduction reaction (ORR). [95] The observation that the CISS effect can enhance both ORR and OER performance naturally points toward its potential relevance for energy systems governed by these reactions. Among them, metal–air batteries (MABs) - which fundamentally rely on ORR during discharge and OER during recharge - have emerged as especially promising candidates, having attracted growing attention in recent years thanks to their high theoretical energy density and several additional advantages (to be further detailed in Section 3.2.1). Despite this promise, the development of MABs is still hindered by persistent safety and performance limitations. In this context, the CISS effect offers an intriguing opportunity, as it may provide a novel pathway to mitigate these challenges and advance the practical realization of metal–air battery technologies.

With this perspective in mind, the next section begins by taking a closer look at metal–air batteries, exploring their fundamental operating principles and key characteristics. From there, we turn to an exciting possibility: how the CISS effect could be leveraged to enhance the efficiency of their essential electrochemical reactions, offering a promising route to overcome some of the limitations that have so far constrained the full potential of these systems.

 doi:10.20944/preprints202603.2520.v1

3.2. Metal-Air Batteries

3.2.1. Metal–Air Batteries: Key Features, Current Status and Practical Challenges

Overview

While lithium-ion batteries (LIBs) currently lead the market in terms of performance, challenges remain—particularly in achieving high capacities (>200 mA h g^{-1}) and ensuring safe operation for electric vehicle (EVs) applications [96–98]. In this context, metal–air batteries have garnered increasing attention due to their ability to operate under ambient air conditions. In contrast to LIBs, which rely on costly and often resource-limited materials, MABs offer a more economical alternative by using abundant atmospheric oxygen as the cathode reactant and low-cost metals - such as aluminum, zinc, or iron - as anodes. The combination of cost-effectiveness, high theoretical energy density, and markedly reduced overall weight positions MABs as highly promising candidates for compact power sources in portable electronics and EVs. Beyond these applications, MABs also show strong potential for large-scale energy storage and distribution, [99] serving as efficient energy transfer hubs within integrated renewable energy systems. In such architectures, they could enable seamless energy exchange among renewable sources such as wind and solar power, the electrical grid, and end users.

Components and Configuration

Unlike conventional closed systems, MABs typically operate in an open-cell configuration, and comprise three principal components, as schematically illustrated in Figure 8a: a metal anode, a porous air cathode, and an electrolyte that separates the electrodes. The anode is generally composed of metals such as lithium (Li), sodium (Na), potassium (K), magnesium (Mg), aluminum (Al), iron (Fe), or zinc (Zn), chosen based on energy density requirements, electrochemical stability, and cost considerations. MABs employ a range of electrolytes, most commonly aqueous and non-aqueous (aprotic) systems, while solid-state and hybrid designs have more recently emerged as promising directions.[100,101]. Due to their high reactivity with water, lithium–air, sodium–air, and potassium–air batteries are commonly paired with non-aqueous electrolytes to prevent undesirable side reactions. In contrast, magnesium-, aluminum-, iron-, and zinc-based systems are compatible with aqueous electrolytes, though the incorporation of a hydrophobic protective layer is often necessary to mitigate electrolyte leakage and enhance long-term operational stability.[100,102,103] Figure 8b illustrates the operation of MABs in both aqueous and non-aqueous electrolytes.

Structural Design

Based on structural design and operational requirements, MABs are classified into conventional static configurations, flow-based systems, and advanced flexible architectures[104] (Figure 8c).

Traditional static MABs: conventional static metal–air batteries consist of a cathode, separator, electrolyte, and anode. While the metal anode oxidation (e.g., $Zn \rightarrow Zn^{2+} + 2e^-$) proceeds with relatively fast kinetics, the ORR at the cathode is intrinsically sluggish due to its multi-electron transfer pathway. During discharge, the ORR occurs at the three-phase interface formed by the solid catalyst, liquid electrolyte, and gaseous oxygen, whereas during charging, the OER takes place at the two-phase catalyst–electrolyte interface. [105]. Hence, the development of highly active bifunctional catalysts is essential to facilitate both ORR and OER efficiently. Furthermore, the use of liquid electrolytes often leads to the formation of insoluble by-products (e.g., ZnO, Li_2O_2) on electrode surfaces during cycling. These deposits obstruct the porous electrode structure, restrict oxygen diffusion, and ultimately deteriorate the overall electrochemical performance [106].

Flow-electrolyte MABs: This configuration incorporates an electrode, separator, electrolyte, and an external electrolyte reservoir, with a pump integrated to maintain continuous electrolyte circulation. Such a flowing-electrolyte system mitigates several limitations of static designs, particularly at the metal anode and air cathode interfaces. More specifically, the flowing-electrolyte

 doi:10.20944/preprints202603.2520.v1

design mitigates irregular anode morphology, and passivation by maintaining uniform ion concentration and reducing polarization effects. For instance, in zinc–nickel batteries, electrolyte circulation minimizes dendrite formation and irregular zinc morphology by improving ion distribution, reducing concentration gradients, and preventing passivation[107] .

However, in this kind of configuration optimal electrolyte flow rates are critical for balancing mass transport and energy efficiency. Insufficient flow leads to concentration polarization and localized depletion of active species, while excessive flow increases parasitic energy losses due to pumping requirements and reduces volumetric energy density. Furthermore, mass transport processes at the electrode–electrolyte interface strongly influences redox kinetics and overall battery performance, emphasizing the need for precise hydrodynamic and electrochemical design to achieve stable long-term cycling. Nonetheless, this architecture introduces additional drawbacks, primarily the increased system complexity associated with integrating pumps, tubing, and flow control mechanisms required to sustain electrolyte circulation.

Flexible MABs: The growing demand for portable electronics has stimulated significant research into lightweight, compact, and flexible batteries [108,109]. A typical flexible battery comprises a cathode, anode, separator, and a highly conductive electrolyte, with solid-state electrolytes being the most commonly employed. To date, thin metallic plates are often utilized as anodes to reduce overall battery weight, while various nanomaterials and nanocomposites - such as carbon fibers, carbon nanotubes, and graphene - are explored as cathode materials. Current developments indicate an evolutionary trajectory from polymer and flexible alkaline batteries to lithium-based and metal–air batteries, which represent a particularly promising class of flexible energy storage devices. Flexible metal–air batteries combine the high theoretical energy density of metal–air chemistries with mechanical flexibility, enabling their integration into wearable and foldable electronics. These systems typically employ a metal anode, a breathable air cathode, and a flexible electrolyte, which allows them to sustain energy output even under bending or stretching conditions, making them highly suitable for next-generation portable applications. Despite their potential, challenges such as mechanical durability, electrolyte stability, and consistent cycling performance under repeated deformation remain. Currently, zinc–air (ZABs) and aluminum–air batteries (AABs) are among the most promising flexible systems, combining low cost, safety, and high energy density [110].

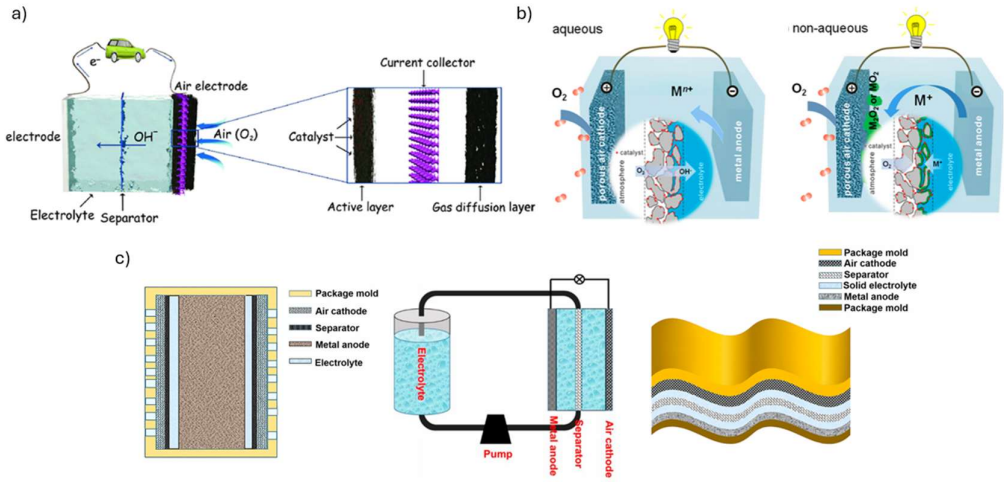

Figure 8. a) Schematic illustration of a MAB. Adapted from Ref.[111] under terms of the CC-BY license. b) Schematic diagrams of MABs working principles for aqueous and non-acqueous electrolyte. Adapted from Ref.[112]. © 2025 MDPI. c) Illustration of various MAB designs: static multi-cell arrangement (left), flow-type battery system (middle), and flexible (right) battery structure (modified). Adapted from Ref.[96] under terms of the CC-BY license.

 doi:10.20944/preprints202603.2520.v1

Electrochemical Reaction Mechanisms in Metal–Air Batteries

The working principles of metal–air batteries differ significantly from that of conventional ionic batteries. In traditional systems, metallic ions are transferred from the anode to the cathode during operation. In contrast, MABs rely on the oxidation of a metal or alloy at the anode to produce metallic ions and electrons, while oxygen is reduced at the cathode [113] to form hydroxide or oxygen-containing anions, depending on the electrolyte system. In other words: during the oxidation of the metal anode, metallic ions are generated, accompanied by the release of electrons, which then flow through the external circuit to deliver electrical energy. The resulting metallic ions subsequently dissolve into the electrolyte, completing the discharge process (Figure 9a). In rechargeable MABs, the reactions are reversed upon charging, with metallic ions being reduced back to the metal state at the anode, thereby restoring the cell to its original condition[114]. The degree of reversibility and efficiency of these electrochemical processes plays a crucial role in determining battery performance, affecting aspects such as capacity, cycle stability, energy efficiency, and degradation pathways [95]. In contrast to traditional batteries, which contain both anode and cathode reactants internally, MABs draw oxygen from the surrounding air to serve as the cathode reactant: oxygen enters the system through the gas diffusion layer (Figure 9a), which regulates its transport to the cathode and facilitates the oxygen ORR. This distinct electrochemical mechanism lowers the overall battery mass and underpins the high energy density characteristic of MABs, positioning metal–air systems as strong contenders for advanced energy storage applications. Notably, the behavior of oxygen differs between aqueous and non-aqueous electrolytes, influencing reaction kinetics and overall cell performance.

In an aqueous electrolyte, oxygen diffuses through the gas diffusion layer and undergoes reduction to hydroxide ions (OH^-) via a multi-electron pathway[112,113] :

$$O_2 + 2H_2O + ne^- \rightarrow 4OH^-$$

In non-aqueous electrolytes, oxygen reduction first leads to the formation of superoxide (O_2^-) species, which acts as a reactive precursor:

$$O_2 + e^- \rightarrow O_2^-$$

Depending on the metal's reactivity, electrolyte environment, and electrochemical conditions, this superoxide may either remain as a soluble intermediate, $O_2^- + M^+ \rightarrow MO_2$, disproportionate to form a peroxide (O_2^{2-}), $2MO_2 \rightarrow M_2O_2 + O_2$, or undergo further reduction to form a stable metal oxide, $MO_2 + 2e^- + 2M^+ \rightarrow M_2O_x$. This sequence determines the nature of the final solid discharge product and strongly influences energy density, rechargeability, and cycle life.

Simultaneously, metals at the anode release electrons, forming metallic ions, which subsequently dissolve into the electrolyte:

$$M \rightarrow M^{n+} + ne^- \text{ (aqueous) } M \rightarrow M^+ + e^- \text{ (non-aqueous)}$$

During charging, these electrochemical processes are reversed, with metallic ions reduced back to the metal state and oxygen evolved at the cathode via the OER. The initial state of the electrodes and electrolyte are thus restored, thereby enabling rechargeable MAB operation. Table 2 provides an overview of the key electrochemical reactions in representative metal–air battery systems, detailing the anode and cathode processes and the corresponding primary discharge products for both aqueous and non-aqueous electrolytes.

Table 2. Electrochemical Reactions in Representative Metal–Air Batteries[115–125].

Battery System	Electrolyte Type	Anode Reaction (Discharge)	Cathode Reaction (Discharge)	Key Products
Zn–Air	Aqueous	$Zn \rightarrow Zn^{2+} + 2e^-$	$O_2 + 2H_2O + 4e^- \rightarrow 4OH^-$	$Zn(OH)_2$ / ZnO
Al–Air	Aqueous	$Al \rightarrow Al^{3+} + 3e^-$	$O_2 + 2H_2O + 4e^- \rightarrow 4OH^-$	$Al(OH)_3$
Li–Air	Non-Aqueous	$Li \rightarrow Li^+ + e^-$	$O_2 + 2Li^+ + 2e^- \rightarrow Li_2O_2$	Li_2O_2
Na–Air	Non-Aqueous	$Na \rightarrow Na^+ + e^-$	$O_2 + 2Na^+ + 2e^- \rightarrow Na_2O_2$	Na_2O_2

 doi:10.20944/preprints202603.2520.v1

Fe–Air	Aqueous	$Fe \rightarrow Fe^{2+} + 2e^-$	$O_2 + 2H_2O + 4e^- \rightarrow 4OH^-$	$Fe(OH)_2$

The electrolyte medium strongly influences oxygen transport, reaction kinetics, and discharge products. Aqueous systems generally offer higher ionic conductivity and lower overpotentials, while non-aqueous systems enable the use of highly reactive metals such as lithium and sodium, albeit with reduced rechargeability due to passivation and parasitic reactions.

Performances

Theoretical energy density is a key parameter in assessing the performance potential of different battery chemistries and, as anticipated, these batteries are attractive due to their exceptionally high theoretical energy densities, usually exceeding those of state-of-the-art technologies (Figure 9b), up to 1000 Wh kg^{-1} and 5000 Wh L^{-1} with respect to the lithium-ion at a material level [126,127].

Various MAB systems differ significantly in their theoretical energy density, specific energy, and nominal cell voltage [128] (Figure 9c). Among the different configurations, lithium–air batteries (LABs) stand out for offering the highest theoretical energy density (5928 Wh kg^{-1}) and a relatively high nominal cell voltage of approximately 2.96 V. In contrast, iron–air batteries (FABs) exhibit the lowest theoretical energy density and a nominal voltage of around 1.28 V. Despite this, Al–air, Zn–air, and Fe–air batteries continue to attract considerable research interest due to their favorable safety profiles, material abundance, and cost-effectiveness, which make them promising candidates for scalable and sustainable energy storage solutions.

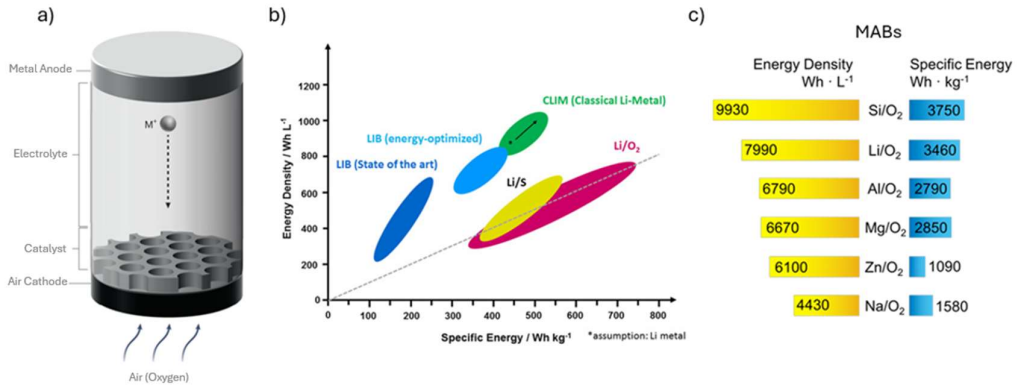

Figure 9. a) Schematic representation of a Metal-air battery. Adapted from Ref.[129]. Springer Nature. b) Energy density vs. specific energy plot comparing current-generation lithium-ion batteries, energy-optimized LIBs, lithium-metal batteries and post-lithium-ion technologies, including lithium–sulfur (Li/S) and lithium–oxygen (Li/O_2) systems, at the cell level. The dotted gray line indicates the parity between energy density and specific energy (i.e., Wh/L = Wh/kg). Data are partially adapted from reference [130]. Adapted from Ref.[131]. Springer Nature. c) Theoretical energy density and specific energy (including atmospheric oxygen) for commonly studied metal–air batteries. The values are derived based on the mass and volume of the discharge products, the open-circuit voltage (OCV), and the total charge transferred during the cell reaction. Adapted from Ref.[128] under terms of the CC-BY license.

Actual Limitation and Future Perspective

Despite their theoretical advantages, metal–air technologies still face significant technical and commercialization challenges, most notably the thermodynamic and the sluggish kinetics of the ORR and OER half-reactions,[132,133] which govern round-trip efficiency, attainable energy density, and overall electrochemical performance of the system. Specifically, ORR activity directly influences discharge efficiency, whereas OER kinetics govern rechargeability and cycle stability. Moreover, the role of H_2O in the discharge and charge processes remains complex and is not yet fully understood[134–136]. Owing to the intrinsically slow multi-electron transfer kinetics and high overpotentials associated with both ORR and OER (vide Section 3.2.2), the deployment of highly

 doi:10.20944/preprints202603.2520.v1

active electrocatalysts is indispensable to reduce polarization losses and enhance reaction kinetics. Although noble metals such as Platinum (Pt), Iridium (Ir), and Ruthenium (Ru) remain benchmark catalysts, their scarcity and prohibitive cost significantly constrain large-scale implementation. Consequently, extensive efforts have been directed toward the rational design of cost-effective catalyst systems, including transition-metal oxides, perovskite-type oxides, and other nanostructured materials, to achieve high activity, durability, and bifunctionality. These barriers in term of performance and limited cycle life, coupled with the need for cost reductions and standardized supply chains, have so far restricted deployments to pilot or demonstration scales [96,137]. Near-term developments (1–5 years) are expected to focus on pilot projects and scaling promising chemistries, while medium-term commercial viability (5–10 years) will depend on achieving reliable cycle life, air-cathode durability, and cost competitiveness.

While conventional approaches - ranging from catalyst composition and nanostructuring to interface engineering and electronic structure tuning - have yielded important advances, they still fall short of fully overcoming these intrinsic limitations, fundamentally constrained by the inherent reaction pathways. In this context, the CISS effect can be considered a potentially transformative strategy, as current evidence - further elaborated in Section 3.2.2. - suggests it may leverage spin-polarized electron transport to intrinsically enhance reaction kinetics and reduce side reactions in MABs[138–140]. Unlike traditional approaches that primarily target surface chemistry, through CISS effect it may be possible to manipulate spin polarization at electrode–electrolyte interfaces, thereby modulating reaction intermediates, lowering activation barriers, and steering product distribution toward more desirable pathways[58,91,141]. In other words, CISS directly addresses spin-dependent processes at the heart of ORR and OER, enabling higher activity, improved stability, and reduced energy losses. Moreover, chiral modifiers on cathode surfaces could serve both as spin filters and as catalytic sites, offering a dual-function strategy for performance enhancement. This emerging paradigm introduces opportunities for rational catalyst design that integrates spintronic principles with traditional electrochemical strategies, potentially leading to significant performance improvements in next-generation metal–air battery technologies.

Its distinctive mechanism positions CISS not merely as an alternative, but as a potentially superior strategy with the capacity to redefine electrocatalyst design and unlock the requirements for practical next-generation MABs. Though so promising, it is worth noting that the integration of CISS-active interfaces into metal-air battery architectures remains an emerging research direction. However, preliminary studies in related electrochemical systems suggest that chiral molecules can influence the rate and directionality of oxygen-related redox processes[141] , making this an exciting frontier for future exploration.

3.2.2. Metal-Air Batteries, CISS Effect in MABs

CISS Effect on OER

In rechargeable metal–air batteries, the OER takes place during the charging process [142] and involves the oxidation of hydroxide ions or oxides back to molecular oxygen, accompanied by the release of electrons into the external circuit.

The OER plays a critical role in determining the charge efficiency and cycling stability of rechargeable metal-air batteries, as it governs the regeneration of oxygen during the charging process. However, the intrinsically sluggish kinetics of OER result in high overpotentials, leading to significant energy losses and reduced overall efficiency [143]. The slow reaction rate also limits charge acceptance, making rapid and efficient recharging challenging. Addressing these limitations requires the development of highly active and durable catalysts. Consequently, enhancing OER kinetics remains a central research focus for improving the performance and commercial viability of rechargeable MABs. Figure 10a illustrates the OER in an alkaline medium, depicting the stepwise oxidation of hydroxide ions (OH^-) to molecular oxygen (O_2) with associated electron transfer, and here reported:

 doi:10.20944/preprints202603.2520.v1

$$4OH^- \rightarrow O_2 + 2H_2O + 4e^-$$

The CISS effect can play a significant role also in modulating the OER by influencing the spin orientation of electrons during the reaction[144]. In electrocatalytic OER, the multi-step transfer of electrons is inherently coupled with the formation of spin-sensitive intermediates, such as hydroxyl (OH•), oxyl (O•), and peroxo (OOH•) radicals. By introducing chiral molecules onto the electrode surface, the CISS effect induces spin polarization in the electron flow, aligning electron spins with the spin state of the catalytic active sites. [138,145–148] This spin alignment reduces spin-related energy barriers, facilitating faster and more efficient electron transfer, lowering the overpotential, and enhancing the overall reaction kinetics.

Liang et al. (2022) reported a striking demonstration of how the CISS effect can enhance the OER through molecular functionalization of hybrid 2D electrodes[94]. By intercalating helicene derivatives such as thiadiazole-[7]helicene and bis(thiadiazole)-[8]helicene between a gold substrate and Ni/NiFe oxide catalyst islands, they observed up to ~130% enhancement in OER current density compared to non-functionalized systems, along with suppression of parasitic hydrogen peroxide formation. The key to this improvement lies not in altered adsorption energies of intermediates but in the spin polarization generated when electrons traverse the chiral molecules. This spin selectivity directly influences the spin-sensitive OER pathway, particularly the coupling of oxygen atoms into triplet O_2, thereby lowering kinetic barriers and steering the reaction toward the four-electron pathway (Figure 10b). Importantly, electrode architecture was found to be critical, as the chiral layer must act as an interfacial spin polarizer without blocking catalytically active sites. Control experiments with achiral analogues confirmed that the enhancement arises uniquely from chirality and the associated CISS mechanism. Collectively, these findings exemplify how CISS can be deliberately exploited to circumvent conventional scaling limitations in OER catalysis and point toward new design principles for enhancing the efficiency and selectivity of metal-air battery systems.

While Liang et al. (2022) demonstrated that chiral molecular functionalization at the electrode-catalyst interface can induce spin polarization and thereby enhance OER activity and selectivity, Vadakkayil et al. (2023) extended this principle by directly embedding chirality into the catalyst lattice itself, synthesizing chiral $Co_{(3-x)}Fe_xO_4$ nanoparticles (notably $Co_{2.3}Fe_{0.7}O_4$) and comparing them with achiral counterparts[149]. The chiral catalysts exhibited markedly lower overpotentials, higher Faradaic efficiencies, several-fold gains in mass and specific activities, and reduced hydrogen peroxide production, especially under acidic conditions. Kinetic analysis revealed a shift in the rate-determining step, consistent with spin polarization altering the reaction pathway. The proposed mechanism is that CISS injects spin-down electrons into the catalyst, producing spin-up surface intermediates (M–O• radicals) that align with the triplet ground state of O_2, thereby bypassing spin-forbidden transitions. Notably, these improvements arose even though the achiral catalysts already operated near the volcano-plot apex, underscoring that spin control provides a design lever beyond adsorption-energy optimization. This work highlights the potential of embedding chirality into catalyst materials to intrinsically bias spin, reinforcing CISS as a general strategy to achieve superior OER performance in metal–air batteries.

Taken together, these studies illustrate two complementary strategies by which the CISS effect can be harnessed to improve OER catalysis. The former highlights how chiral molecular layers at the electrode-catalyst interface can act as spin filters that polarize charge transfer without altering the intrinsic catalyst composition, while the latter demonstrates that chirality embedded directly into the catalyst lattice itself can create intrinsically spin-polarized active sites. This is the demonstration that CISS can operate across different length scales and architectures: from molecular assemblies that modulate electron spin at interfaces to bulk catalysts whose chiral crystal structure governs spin-selective charge transfer and intermediate formation. Despite their different approaches—interfacial versus structural chirality—both converge on the same mechanistic principle: spin polarization

 doi:10.20944/preprints202603.2520.v1

stabilizes radical-type intermediates consistent with the triplet ground state of O_2, thereby lowering kinetic barriers and surpassing the conventional activity limits dictated by adsorption-energy scaling.

This dual perspective underscores the versatility of CISS as a unifying design principle for next-generation OER catalysts and highlights its promise for advancing the performance of metal-air batteries.

CISS Effect on ORR

A comprehensive understanding of how the CISS effect can enhance ORR performance requires first an examination of the two mechanistic pathways possible at the cathode, since the pathway by which this reaction proceeds critically determines the efficiency, stability, and overall performance of MABs. Mechanistically, ORR can follow two distinct routes [95] :

a) Two-Electron Pathway

$$O_2 + 2e^- + 2H^+ \rightarrow H_2O_2 \text{ or } O_2 + 2e^- + H_2O \rightarrow HO_2^- + OH^- \text{ when in alkaline electrolytes}$$

b) Four-Electron Pathway

$$O_2 + 4e^- + 4H^+ \rightarrow 2H_2O \text{ or } O_2 + 4e^- + 2H_2O \rightarrow 4OH^- \text{ when in alkaline electrolytes}$$

In the two-electron ($2e^-$) pathway, hydrogen peroxide (H_2O_2) or its anionic form (HO_2^-) is generated as an intermediate. The formation of these peroxides presents major challenges, as their intrinsic instability leads to decomposition into water and oxygen, causing parasitic energy losses. Additionally, peroxide intermediates trigger undesirable side reactions that accelerate electrode degradation, surface passivation, and corrosion, ultimately limiting the cycle life of rechargeable MABs [150–152]. To mitigate these effects, catalysts are required either to suppress peroxide formation by favoring the four-electron pathway or to rapidly decompose peroxides.[153].

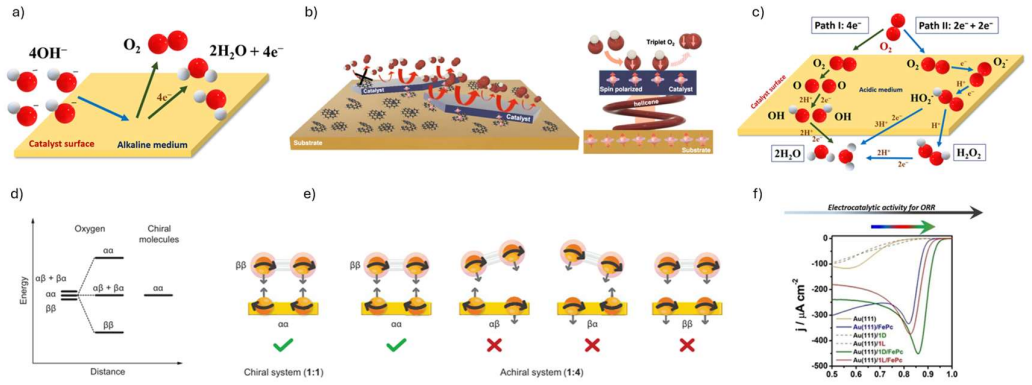

Figure 10. a) Schematic illustration of the OER in an alkaline medium, depicting the oxidation of hydroxide ions (OH^-) to molecular oxygen (O_2) with associated electron transfer, Adapted from Ref.[95], with permission from Elsevier. b) Effect of chiral molecules on OER activity, highlighting how spin polarization influences reaction pathways. Adapted from Ref.[94] under terms of the CC-BY license. c) ORR two- and four-electron pathway in acidic medium, producing peroxide and water, respectively. Adapted from Ref.[95], with permission from Elsevier. d) The splitting of the spin states of triplet oxygen due to interaction with the spin-polarized electrons present on chiral molecules. e) Interaction of triplet oxygen with spin-polarized electrons on chiral and achiral molecules. In achiral systems, the two electrons can adopt four spin configurations, but only one leads to a reaction. In chiral systems, a single strongly coupled configuration exists, which exclusively drives the reaction. (d-e) Adapted from Ref.[3] under the terms of the Creative Commons CC-BY-NC-ND 4.0 License. f) Linear Sweep Voltammetry (LSV) for ORR on CSA(D and L) FePcs, performed in 0.1 M NaOH saturated with O_2. Adapted from Ref.[154]. © Wiley 2024.

 doi:10.20944/preprints202603.2520.v1

The four-electron ($4e^-$) pathway is the preferred mechanism in rechargeable MABs, as it directly reduces oxygen to water or hydroxide ions without generating harmful peroxide species [155]. This direct reduction maximizes electron transfer, thereby enhancing energy efficiency, increasing energy density, and minimizing side reactions that could degrade electrode materials. Figure 10c schematically illustrates the two-electron and four-electron ORR pathways in an acidic medium. Despite its advantages, the four-electron pathway suffers from inherently sluggish kinetics, which can limit power output and overall efficiency if not properly addressed. Effective catalysts are therefore indispensable for accelerating the reaction, reducing energy losses, and ensuring high-performance operation [156].

The possible influence of spin polarization on the oxygen reduction reaction arises from the spin-dependent nature of electron transfer to molecular oxygen. Regardless of the specific mechanistic pathway, the initial step of ORR requires the transfer of at least two electrons to form either O_2^{2-} or HO_2^- [3,157]. From a spin-statistical perspective, the critical factor is the projection of the oxygen molecule's spin onto the chiral axis of the molecular layer as O_2 approaches the electrode. Because oxygen contains two unpaired electrons, three spin configurations are possible: $\alpha(1)\alpha(2)$, $\beta(1)\beta(2)$, and the mixed state $[\alpha(1)\beta(2) + \beta(1)\alpha(2)]/\sqrt{2}$. In the presence of chiral molecular layers, the injected electrons are spin-polarized along the molecular axis, favoring the $\alpha\alpha$ configuration. This selectivity modifies the reaction barrier through both entropic contributions, linked to spin statistics, and enthalpic stabilization of the $\beta(1)\beta(2)$ oxygen state via spin-exchange interactions with polarized electrons. As illustrated schematically in figure 10d, the approach of O_2 to a chiral monolayer lead to the lifting of spin-state degeneracy, akin to the effect of an external magnetic field, with preferential stabilization of the $\beta(1)\beta(2)$ state. Upon closer interaction—where the electron densities of oxygen and the chiral film overlap—these spin-exchange interactions intensify, thereby strongly influencing the ORR pathway. This spin-selective interaction lowers the enthalpic barrier, thereby facilitating more efficient spin injection from the chiral monolayer into the oxygen system. In addition, the alignment of the oxygen spin states with the chiral framework reduces the entropic contribution to the overall free energy barrier. By contrast, in the case of an achiral film, four spin configurations are possible within the monolayer ($\alpha\alpha$, $\beta\beta$, $\alpha\beta$ and $\beta\alpha$), yet only one of these states enables efficient electron transfer to oxygen, limiting the reaction probability to one in four (figure 10e). Furthermore, because the spins in achiral systems are not coupled to a molecular axis, the oxygen spin states remain degenerate and are not energetically stabilized, meaning that the enthalpic barrier is not lowered.

Beyond simply reducing the activation barrier, this spin control has direct consequences for the selectivity of the ORR. The CISS effect, by enforcing spin alignment between injected electrons and oxygen's electronic states, selectively stabilizes the four-electron pathway while disfavoring peroxide formation. In this way, spin polarization not only enhances the kinetics and the selectivity of ORR but – introducing a mechanistic strategy to suppress harmful side reactions and improve battery performance – also ensures a more efficient and safer electrochemical process within metal-air systems.

These mechanistic insights have been substantiated by experimental studies. In 2022, Naaman and co-workers demonstrated that chiral molecular coatings on electrodes significantly enhance ORR activity, providing direct evidence that spin polarization can influence both reaction kinetics and selectivity [3]. More recently, Zheng and colleagues extended this concept to a chiral self-assembled iron phthalocyanine system [154], showing that spin-dependent electrocatalysis can be implemented in transition-metal-based catalysts and well-defined molecular architectures (Figure 10f). Both studies confirm that spin polarization is not merely a theoretical construction but a tunable parameter that can be harnessed to control ORR pathways.

Based on the evidence discussed above regarding ORR and OER, it can be concluded that the integration of spin-selective interactions into electrode architectures can enhance reaction rates, improve selectivity toward desired products, and suppress formation of deleterious intermediates, an approach that opens new avenues for energy storage and conversion technologies.

 doi:10.20944/preprints202603.2520.v1

3.3. Harnessing the CISS Effect in Other Possible Electrocatalytic Reactions for Advanced Energy Storage Systems

While most studies have focused on the role of the CISS effect in oxygen-related reactions such as ORR and OER, emerging evidence suggests that spin-dependent phenomena can also influence other key electrochemical reactions. In particular, CO_2 and nitrogen reduction reactions have recently been identified as promising systems in which spin polarization may modulate catalytic activity and selectivity. Beyond their fundamental significance, these reactions also present opportunities for application in batteries and other energy storage devices. A brief discussion of these effects is provided in Sections 3.3.1. and 3.3.2.

3.3.1. CO_2 Reduction Reaction (CO_2RR) Principles and CISS Effect

The electrochemical CO_2RR offers a promising pathway for converting carbon dioxide into value-added fuels and chemicals, such as CO, formate, methanol, or hydrocarbons [158,159]. This reaction not only offers a pathway for mitigating greenhouse gas emissions but also provides a means to store renewable energy in chemical bonds. Moreover, it represents also a good strategy for storing energy harvested from intermittent renewable sources such as wind and solar power [160].

Despite the promising prospects of the CO_2RR, its widespread implementation is hindered by several critical challenges. The strong stability of CO_2 results in sluggish reaction kinetics, thereby necessitating the design of advanced catalysts capable of efficiently activating the molecule and lowering the overpotentials. These catalysts must simultaneously suppress the competing hydrogen evolution reaction (HER) while ensuring high selectivity toward the targeted reduction products. Maintaining such selectivity, alongside preserving catalytic activity and structural stability over extended operational durations, remains a significant obstacle. Furthermore, the intrinsic complexity of the CO_2RR, which involves multiple coupled proton- and electron-transfer steps, adds an additional layer of difficulty. Consequently, the precise optimization of catalyst surface properties and reaction conditions is indispensable for achieving efficient and durable CO_2 conversion.

Recent advancements have highlighted the potential of the CISS effect to address these challenges, modulating reaction kinetics by promoting spin-polarized electron transfer at chiral catalyst interfaces. [11,161–165]. In this context, since certain CO_2RR intermediates involve unpaired electron configurations, spin polarization may selectively favour desired pathways while suppressing undesired side reactions. This intuition arose from the evidence that applying an external magnetic field can enhance the efficiency of the CO_2RR. For example, in the case of conversion to formic acid, the singlet radical pair configuration ($[CO^{2-\bullet} \uparrow \cdots H^{\bullet} \downarrow]^1$) has been shown to be more favorable than the triplet radical pair configuration ($[CO^{2-\bullet} \uparrow \cdots H^{\bullet} \uparrow]^3$) [166,167]. The application of an external magnetic field can facilitate the transition from triplet to singlet states (Figure 11a), thereby promoting formic acid production, minimizing HER and improving the performance of the CO_2RR. [11,168,169]. These pioneering studies unveiled a novel mechanistic pathway for enhancing the efficiency of the CO_2 reduction reaction.

Since the application of external magnetic fields has demonstrated significant potential in this context, the CISS effect presents an alternative approach for achieving efficient spin polarization, even in diamagnetic materials such as Cu, which has long been recognized as a benchmark catalyst for the electrochemical conversion of CO_2 into valuable hydrocarbon products with notably high Faradaic efficiencies [170–172]. Building upon this understanding, recent advances have demonstrated that chiral Cu-based electrocatalysts exhibit further improvements in Faradaic efficiency and selectivity toward desired carbon products, effects that can be attributed to the CISS-mediated alignment of electron spins and its consequent influence on reaction kinetics (Figure 11b) [173].

Extending beyond copper systems, chiral BiOBr nanospheres have also been shown to deliver enhanced photocatalytic CO_2 reduction activity compared to their achiral counterparts, thereby underscoring the broader role of chirality-induced spin polarization in facilitating charge separation and suppressing charge recombination (Figure 11c,d)[174]. Moreover, this evidence also confirms

 doi:10.20944/preprints202603.2520.v1

that nanoscale architectures constitute an ideal platform for exploiting chirality-induced spin polarization even in the case of CO_2RR, the potential of the CISS effect is amplified when applied to materials at the nanoscale, where structural confinement and high surface-to-volume ratios magnify its impact on charge and spin dynamics.

While the exact mechanisms underlying the CISS effect in CO_2RR are still under investigation, these findings suggest that leveraging spin polarization through chiral catalysts can provide a new dimension in electrocatalytic design, potentially leading to more efficient and selective CO_2 conversion processes. Moreover, the synergy between chirality and nanoscale engineering may serve as a guiding principle for the development of next generation electrocatalysts and photocatalysts, opening new avenues for efficient and sustainable CO_2 conversion.

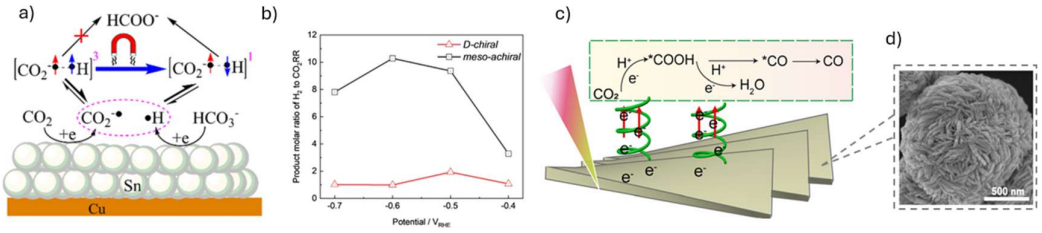

Figure 11. a) Illustration of the proposed generation mechanism for magneto-current driven by electro catalytic CO_2 reduction. Adapted with permission from Ref.[169]. Copyright 2020 American Chemical Society. b) Molar ratio of H_2 to CO_2RR products at various applied potentials for D-chiral and meso-achiral systems. Hydrogen generation is notably reduced on chiral Cu across all potentials. Adapted from Ref.[173]. under terms of the CC-BY license. c) The mechanism for CO_2 photoreduction over D-BiOBr. d) SEMimage of chiral BiOBr. (c,d) Adapted from Ref.[174] Reproduced by permission of The Royal Society of Chemistry.

Looking forward, integrating the CISS effect with CO_2RR presents a transformative pathway for energy technologies. By precisely tuning electron spin during electrochemical reactions, researchers can develop catalysts that not only optimize CO_2 conversion but also seamlessly align with advanced battery architectures. In the not-too-distant future, a compelling prospect is the design of rechargeable metal–CO_2 batteries, where CO_2 is electrochemically reduced during discharge and regenerated upon charging. This approach directly supports the broader vision of sustainable, high-efficiency energy solutions capable of addressing both environmental and technological challenges. Similarly to what occurs with ORR and OER, exploiting the CISS effect in these systems could enhance the efficiency and selectivity of the CO_2RR, leading to improved energy density and cycling stability, facilitating at the same time the formation of specific discharge products, thereby optimizing overall battery operational quality.

3.3.2. Nitrogen Reduction Reaction (NRR) Principles and CISS Effect

While the NRR is primarily explored for sustainable ammonia synthesis [175–182], its integration into battery technologies [183–187] is attracting increasing interest. Drawing inspiration from the dual function of metal-CO_2 batteries - simultaneous gas conversion and electricity generation - researchers are now exploring metal-N_2 battery systems as a means to better harness atmospheric nitrogen. In this case, electrochemical nitrogen fixation can serve as both a method of chemical energy storage and a way to close the nitrogen cycle in a sustainable energy loop.

Structurally analogous to metal-air batteries, metal-N_2 batteries typically consist of a metal anode paired with a cathode coated with an electrocatalyst that facilitates the NRR [188–192]. The redox processes in metal-N_2 batteries are influenced by the nature of the electrolyte, namely whether it is aprotic (Figure 12a,b) or protic (Figure 12c,d). In a nonaqueous metal-N_2 battery, during discharge, nitrogen reduction at the cathode, facilitated by the corresponding metal ions, results in the formation of metal nitrides — e.g. Li_3N, Na_3N, or AlN — which can subsequently be hydrolyzed to produce ammonia [189,190,193]. During charging, under an applied external bias, the nitrides at

 doi:10.20944/preprints202603.2520.v1

the cathode decompose into metal ions and gaseous nitrogen [5,194,195]. The most commonly developed nonaqueous metal-N_2 batteries to date include the Li-N_2, Na-N_2, and Al-N_2 batteries [188,196]. Given the economic, operational, and maintenance challenges associated with aprotic electrolytes, considerable research efforts have been directed toward the development of aqueous metal-N_2 batteries[191,197–202]. In these systems, the cathode undergoes the NRR during discharge and the OER during charge[35] . During discharge, the NRR draws electrons from the oxidized metal anode and protons from the electrolyte, resulting in ammonia formation [34,42] and enabling, as anticipated, the simultaneous production of ammonia and generation of electricity [58,203]. To elucidate the mechanisms and intermediates involved in the NRR process, Figure 12e provides a schematic illustration of the four principal pathways for N_2 reduction and NH_3 synthesis in metal-N_2 batteries[204,205] , while Figure 12f displays the optimized DFT structures of the corresponding reaction intermediates[206].

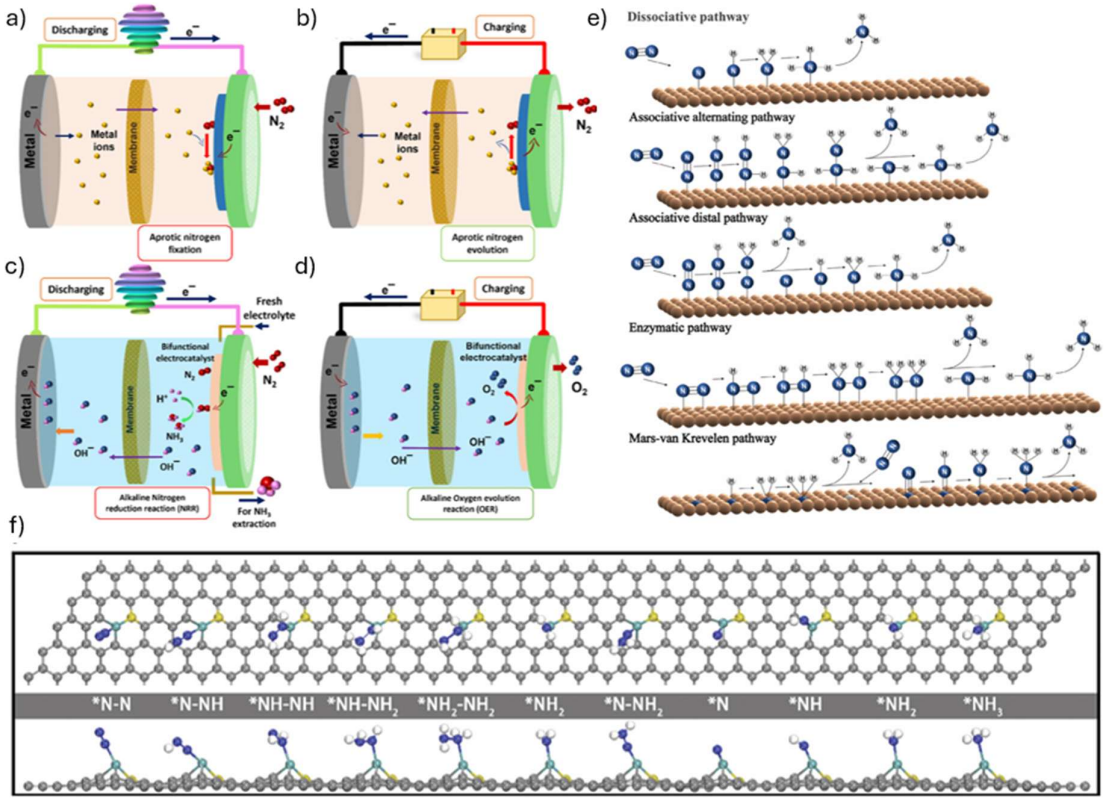

Figure 12. a-d) Representation of the metal–N_2 battery discharge–charge processes in (a, b) aprotic electrolytes and (c, d) alkaline electrolytes. (a-d) Adapted from Ref.[188] under terms of the CC-BY license. e) Illustrative visualization of the possible nitrogen reduction reaction (NRR) mechanisms. Adapted from Ref.[205] under terms of the CC-BY license. f) DFT-optimized geometries of reaction intermediates. (Color legend: Gray – C; Cyan – Metal; Yellow – N; Blue – adsorbed N atoms). Adapted from Ref.[207]. © Wiley 2024.

While these systems hold promise for integrated energy storage and ammonia production, several limitations remain, hindering the NRR efficiency in metal-N_2 batteries. The strong triple bond of N_2 (945 kJ mol^{-1}) poses a significant kinetic barrier, requiring highly active catalysts for effective activation. Furthermore, low N_2 solubility in both aqueous and nonaqueous electrolytes, instability of intermediate species, and the competitive hydrogen evolution reaction (HER)[208,209] — particularly in aqueous systems — undermine selectivity and reduce Faradaic efficiency. Overcoming these challenges is critical to advancing the practical application of metal-N_2 battery technologies. For both systems, efficient, selective, and low-temperature NRR is essential.

 doi:10.20944/preprints202603.2520.v1

Because nitrogen is a diamagnetic molecule and certain NRR steps involve spin-polarized electron transfer, chiral electrodes — whether based on molecular linkers, surface layers, or intrinsically chiral inorganic structures — may guide the reaction toward ammonia production more efficiently, while suppressing the competing HER [210]. Spin polarization has been shown to enhance N_2 adsorption and activation on doped carbon and metal cluster catalysts, lower the Gibbs free energy of intermediates such as NNH*, reduce overall overpotentials, and improve Faradaic efficiencies via spin-selective pathways [11].

By generating spin-polarized electron currents, the CISS effect can lower activation barriers for the rate-determining protonation step ($N_2 \rightarrow NNH^*$) and selectively block electron transfer channels that would otherwise favor HER. This preferential transport of one spin species not only improves selectivity toward ammonia over unwanted side products but also reduces the energetic cost of the reaction. Drawing from analogous successes in ORR and OER — where chiral modifications of catalysts produced significant shifts in onset potentials and enhanced current densities due to spin-polarized charge transfer [194] — it is reasonable to anticipate that similar performance gains could be achieved in NRR, highlighting the broader applicability of CISS principles across multiple electrochemical energy conversion and storage systems.

4. Conclusions and Future Perspectives

The chirality-induced spin selectivity effect, also known as CISS effect and first reported in the early 2000s, describes the ability of chiral molecules to preferentially transmit electrons of a given spin orientation, thereby coupling charge transport with spin polarization. Since its discovery, it has been experimentally demonstrated through photoemission studies, electrochemical measurements, and conductive atomic force microscopy, while advanced techniques such as mc-AFM, circular dichroism, and CISS-induced optical rotation in photoluminescence experiments have enabled its quantitative characterization.

CISS effect represents a transformative paradigm in the field of energy science, offering a spin-selective mechanism to control charge transport at the molecular level. By leveraging the intrinsic spin-filtering properties of chiral molecules, CISS opens new avenues for enhancing catalytic efficiency, reducing energy losses, and enabling spin-polarized electron transfer in energy conversion and storage systems, as schematically summarized in Figure 13. Among the most promising applications, MABs stand out as a compelling platform for CISS exploitation. The integration of chiral interfaces into air electrodes has shown potential to modulate ORR/OER with unprecedented spin selectivity, thereby improving reaction kinetics and selectivity without relying on scarce or expensive catalysts. Recent experimental efforts have demonstrated that chiral layers on metal surfaces can enhance catalytic activity and selectivity by promoting spin-aligned charge transfer. Applying this strategy to the cathode architecture in metal-air batteries could not only improve performance metrics — such as power density, round-trip efficiency, and cycle life — but also advance the development of entirely new classes of low-cost, bio-inspired, and environmentally benign catalysts. As research advances, the strategic incorporation of CISS principles, i.e. embedding spin control into the design of electrode interfaces and reaction pathways, into the design of next-generation metal-air batteries could lead to more efficient, sustainable, and high-performance energy storage solutions—paving the way for a spintronic approach to clean energy technologies. CISS could fundamentally alter how we approach challenges in energy storage, bringing us closer to innovative scalable battery technologies for the future.

Looking ahead, realizing the full potential of the CISS effect in metal-air batteries will require a multidisciplinary approach that combines synthetic chemistry, spintronics, electrochemistry, and materials science. Future research should focus on the rational design of chiral catalysts and electrode architectures, in-situ characterization of spin-polarized processes, and the development of predictive models linking spin dynamics to electrochemical performance. Furthermore, integrating CISS principles into scalable, manufacturable battery systems will be key to translating laboratory

 doi:10.20944/preprints202603.2520.v1

discoveries into real-world applications. If successful, these efforts could redefine fundamental electrochemical paradigms and drive the next generation energy storage systems.

Building on the demonstrated potential of the CISS effect to enhance oxygen electrocatalysis in metal-air batteries, recent studies have begun to explore its application in other spin-dependent reactions, such as the CO_2RR and the NRR. These emerging directions underline the broad utility of CISS effect in enabling novel electrocatalytic pathways, suggesting that CISS-based strategies could open entirely new tracks for designing new multifunctional electrode materials.

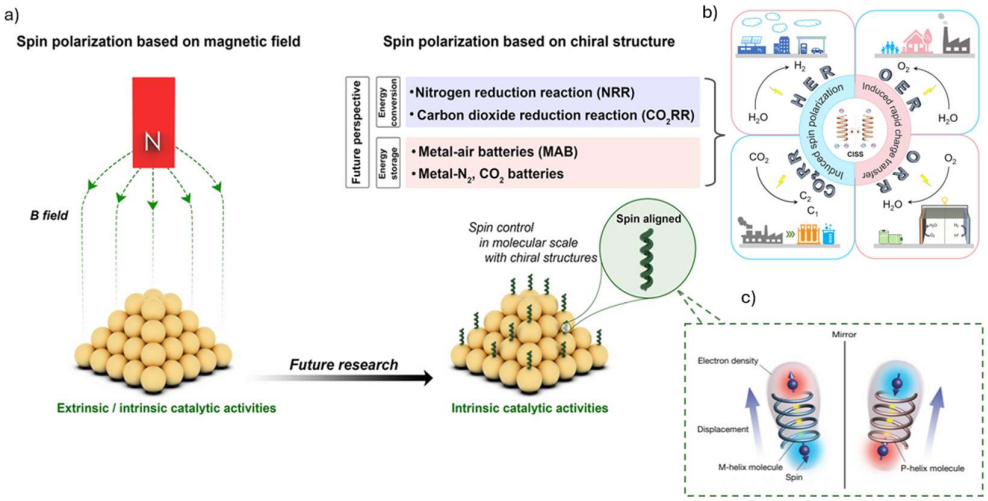

Figure 13. a) Illustration of spin polarization mechanisms in electrocatalysts, achieved through the application of magnetic fields and chiral structures, along with a prospective analysis of their potential impact on energy conversion and storage technologies. Adapted from Ref.[11]. Reproduced by permission of The Royal Society of Chemistry. b) Chiral-induced spin selectivity in electrocatalysis. Adapted from Ref.[211], with permission from Elsevier. c) Representation of antiparallel spins resulting from electron displacement in the CISS. Adapted from Ref.[212]. Springer Nature.

Although direct applications of CISS-enhanced CO_2RR in energy systems are still in the conceptual or early experimental stages, this direction represents a novel and promising pathway for sustainable energy storage. By enabling spin-polarized electron transfer, this approach has the potential to guide the design of catalysts with improved selectivity and efficiency for CO_2 conversion. Although experimental demonstrations remain limited, the prospect of incorporating spin-selective catalysis into devices such as metal–CO_2 batteries, opens new directions for coupling carbon utilization with high-performance energy storage. It is very worth noting that this approach not only advances fundamental understanding of spin-dependent electrocatalysis but also supports the broader transition toward sustainable and carbon-neutral energy systems. As the fundamental understanding of spin-dependent electrocatalysis continues to grow, this strategy may play a key role in the pursuit of sustainable and carbon-neutral energy solutions.

Similar considerations apply to the integration of the CISS effect with the NRR in nitrogen-based batteries, which represents a particularly compelling, though still nascent, direction for energy research. This concept envisions a unified framework that merges green ammonia production, spin-selective chemistry, and electrochemical energy storage into a single platform. Electrochemical ammonia synthesis under mild conditions not only offers a sustainable alternative to the energy-intensive Haber–Bosch process but also introduces the possibility of truly rechargeable ammonia-based energy systems. Within this context, the incorporation of CISS-active materials could play a decisive role by enhancing reaction selectivity and conversion efficiency, thereby enabling more practical nitrogen-to-ammonia energy cycles. The implications extend well beyond incremental performance gains—such as higher energy density, reduced hydrogen evolution losses, and

 doi:10.20944/preprints202603.2520.v1

improved round-trip efficiency—toward the realization of a fully integrated devices where ammonia synthesis and energy storage are seamlessly combined in one device. Such advancements could facilitate applications ranging from distributed power networks and remote energy systems to carbon-free, grid-scale storage solutions. To move from conceptual promise to technological reality, however, it will be essential to combine mechanistic insights — derived from spin-resolved spectroscopy, advanced theoretical modelling, and nanoscale interfacial studies — with breakthroughs in catalyst design, materials engineering, and scalable electrode architectures.

By elucidating the mechanisms underlying CISS, the methods for its measurement, and its application in fundamental processes such as the OER and ORR, this review aims to provide a foundation for future developments in chiral electrochemistry. Beyond these established reactions, the CISS effect holds significant potential for advancing emerging technologies such as NRR and CO_2RR, as well as for improving the efficiency and durability of metal–air batteries, contributing to more sustainable and effective energy systems. Looking ahead, integrating CISS principles into electrocatalysis may not only provide a powerful strategy to overcome current performance limitations but also accelerate broader efforts in renewable energy utilization, paving the way toward a new generation of energy technologies characterized by higher efficiency, sustainability, and multifunctionality. Collaborative efforts across spintronics, catalysis, and energy storage research will be essential to unlock the full potential of spin-selective phenomena in the energy field, pointing toward a future in which energy technologies are both high-performing and environmentally responsible.

Funding: This research was funded by European Union-Next Generation funds through Centro Nazionale per la Mobilità Sostenibile (CNMS), Mission 4, Spoke 13, CN_4 Project (CUP E93C22001070001).

Data Availability Statement: No new data were created or analyzed in this study.

Conflicts of Interest: The Authors declare no conflict of interest.

References

1. Park, Y.S.; Lee, J.; Lee, H.; Park, J.B.; Yun, J.; Lee, C.U.; Moon, S.; Lee, S.; Kim, S.; Kim, J.H.; et al. Elucidating the Chirality-Induced Spin Selectivity Effect of Co-Doped NiO Deposited on Ni Foam for Highly Stable Zn–Air Batteries. *ACS Appl. Mater. Interfaces* **2025**, *17*, 18228–18242, doi:10.1021/acsami.4c20630.
2. Houchins, G.; Pande, V.; Viswanathan, V. Mechanism for Singlet Oxygen Production in Li-Ion and Metal–Air Batteries. *ACS Energy Lett.* **2020**, *5*, 1893–1899, doi:10.1021/acsenergylett.0c00595.
3. Sang, Y.; Tassinari, F.; Santra, K.; Zhang, W.; Fontanesi, C.; Bloom, B.P.; Waldeck, D.H.; Fransson, J.; Naaman, R. Chirality Enhances Oxygen Reduction. *Proc. Natl. Acad. Sci.* **2022**, *119*, e2202650119, doi:10.1073/pnas.2202650119.
4. Ray, K.; Ananthavel, S.P.; Waldeck, D.H.; Naaman, R. Asymmetric Scattering of Polarized Electrons by Organized Organic Films of Chiral Molecules. *Science* **1999**, *283*, 814–816, doi:10.1126/science.283.5403.814.
5. Naaman, R.; Waldeck, D.H. Chiral-Induced Spin Selectivity Effect. *J. Phys. Chem. Lett.* **2012**, *3*, 2178–2187, doi:10.1021/jz300793y.
6. Bloom, B.P.; Paltiel, Y.; Naaman, R.; Waldeck, D.H. Chiral Induced Spin Selectivity. *Chem. Rev.* **2024**, *124*, 1950–1991, doi:10.1021/acs.chemrev.3c00661.
7. Guijarro, A. *The Origin of Chirality in the Molecules of Life: From Awareness to the Current Theories and Perspectives of This Unsolved Problem*; 2nd ed.; The Royal Society of Chemistry, 2022; ISBN 978-1-83916-234-3.
8. He, S.; Chen, Y.; Fang, J.; Liu, Y.; Lin, Z. Optimizing Photocatalysis via Electron Spin Control. *Chem. Soc. Rev.* **2025**, *54*, 2154–2187, doi:10.1039/D4CS00317A.
9. Privitera, A.; Faccio, D.; Giuri, D.; Latawiec, E.I.; Genovese, D.; Tassinari, F.; Mummolo, L.; Chiesa, M.; Fontanesi, C.; Salvadori, E.; et al. Challenges in the Direct Detection of Chirality-induced Spin Selectivity: Investigation of Foldamer-based Donor-acceptor Dyads. *Chem. – Eur. J.* **2023**, *29*, e202301005, doi:10.1002/chem.202301005.

 doi:10.20944/preprints202603.2520.v1

10. Naaman, R.; Waldeck, D.H. Spintronics and Chirality: Spin Selectivity in Electron Transport Through Chiral Molecules. *Annu. Rev. Phys. Chem.* **2015**, *66*, 263–281, doi:10.1146/annurev-physchem-040214-121554.
11. Chae, K.; Mohamad, N.A.R.C.; Kim, J.; Won, D.-I.; Lin, Z.; Kim, J.; Kim, D.H. The Promise of Chiral Electrocatalysis for Efficient and Sustainable Energy Conversion and Storage: A Comprehensive Review of the CISS Effect and Future Directions. *Chem. Soc. Rev.* **2024**, *53*, 9029–9058, doi:10.1039/D3CS00316G.
12. Fu, W.; Tan, L.; Wang, P. Chiral Inorganic Nanomaterials for Photo(Electro)Catalytic Conversion. *ACS Nano* **2023**, *17*, 16326–16347, doi:10.1021/acsnano.3c04337.
13. Mukhina, M.V.; Maslov, V.G.; Baranov, A.V.; Fedorov, A.V.; Orlova, A.O.; Purcell-Milton, F.; Govan, J.; Gun'ko, Y.K. Intrinsic Chirality of CdSe/ZnS Quantum Dots and Quantum Rods. *Nano Lett.* **2015**, *15*, 2844–2851, doi:10.1021/nl504439w.
14. Chen, C.-C.; Zhu, C.; White, E.R.; Chiu, C.-Y.; Scott, M.C.; Regan, B.C.; Marks, L.D.; Huang, Y.; Miao, J. Three-Dimensional Imaging of Dislocations in a Nanoparticle at Atomic Resolution. *Nature* **2013**, *496*, 74–77, doi:10.1038/nature12009.
15. Dong, Z.; Ma, Y. Atomic-Level Handedness Determination of Chiral Crystals Using Aberration-Corrected Scanning Transmission Electron Microscopy. *Nat. Commun.* **2020**, *11*, 1588, doi:10.1038/s41467-020-15388-5.
16. Li, G.; Fei, X.; Liu, H.; Gao, J.; Nie, J.; Wang, Y.; Tian, Z.; He, C.; Wang, J.-L.; Ji, C.; et al. Fluorescence and Optical Activity of Chiral CdTe Quantum Dots in Their Interaction with Amino Acids. *ACS Nano* **2020**, *14*, 4196–4205, doi:10.1021/acsnano.9b09101.
17. Cheng, J.; Hao, J.; Liu, H.; Li, J.; Li, J.; Zhu, X.; Lin, X.; Wang, K.; He, T. Optically Active CdSe-Dot/CdS-Rod Nanocrystals with Induced Chirality and Circularly Polarized Luminescence. *ACS Nano* **2018**, *12*, 5341–5350, doi:10.1021/acsnano.8b00112.
18. Li, Y.; Cheng, J.; Li, J.; Zhu, X.; He, T.; Chen, R.; Tang, Z. Tunable Chiroptical Properties from the Plasmonic Band to Metal–Ligand Charge Transfer Band of Cysteine-Capped Molybdenum Oxide Nanoparticles. *Angew. Chem.* **2018**, *130*, 10393–10397, doi:10.1002/ange.201806093.
19. Kuznetsova, V.A.; Mates-Torres, E.; Prochukhan, N.; Marcastel, M.; Purcell-Milton, F.; O'Brien, J.; Visheratina, A.K.; Martinez-Carmona, M.; Gromova, Y.; Garcia-Melchor, M.; et al. Effect of Chiral Ligand Concentration and Binding Mode on Chiroptical Activity of CdSe/CdS Quantum Dots. *ACS Nano* **2019**, *13*, 13560–13572, doi:10.1021/acsnano.9b07513.
20. Lee, H.-E.; Ahn, H.-Y.; Mun, J.; Lee, Y.Y.; Kim, M.; Cho, N.H.; Chang, K.; Kim, W.S.; Rho, J.; Nam, K.T. Amino-Acid- and Peptide-Directed Synthesis of Chiral Plasmonic Gold Nanoparticles. *Nature* **2018**, *556*, 360–365, doi:10.1038/s41586-018-0034-1.
21. Ohnoutek, L.; Kim, J.-Y.; Lu, J.; Olohan, B.J.; Răsădean, D.M.; Dan Pantoș, G.; Kotov, N.A.; Valev, V.K. Third-Harmonic Mie Scattering from Semiconductor Nanohelices. *Nat. Photonics* **2022**, *16*, 126–133, doi:10.1038/s41566-021-00916-6.
22. Ni, B.; Mychinko, M.; Gómez-Graña, S.; Morales-Vidal, J.; Obelleiro-Liz, M.; Heyvaert, W.; Vila-Liarte, D.; Zhuo, X.; Albrecht, W.; Zheng, G.; et al. Chiral Seeded Growth of Gold Nanorods Into Fourfold Twisted Nanoparticles with Plasmonic Optical Activity. *Adv. Mater.* **2024**, *36*, 2312066, doi:10.1002/adma.202312066.
23. Yan, W.; Xu, L.; Xu, C.; Ma, W.; Kuang, H.; Wang, L.; Kotov, N.A. Self-Assembly of Chiral Nanoparticle Pyramids with Strong *R* / *S* Optical Activity. *J. Am. Chem. Soc.* **2012**, *134*, 15114–15121, doi:10.1021/ja3066336.
24. Lan, X.; Lu, X.; Shen, C.; Ke, Y.; Ni, W.; Wang, Q. Au Nanorod Helical Superstructures with Designed Chirality. *J. Am. Chem. Soc.* **2015**, *137*, 457–462, doi:10.1021/ja511333q.
25. Kuzyk, A.; Schreiber, R.; Zhang, H.; Govorov, A.O.; Liedl, T.; Liu, N. Reconfigurable 3D Plasmonic Metamolecules. *Nat. Mater.* **2014**, *13*, 862–866, doi:10.1038/nmat4031.
26. Ma, L.; Liu, Y.; Han, C.; Movsesyan, A.; Li, P.; Li, H.; Tang, P.; Yuan, Y.; Jiang, S.; Ni, W.; et al. DNA-Assembled Chiral Satellite-Core Nanoparticle Superstructures: Two-State Chiral Interactions from Dynamic and Static Conformations. *Nano Lett.* **2022**, *22*, 4784–4791, doi:10.1021/acs.nanolett.2c01047.
27. Bloom, B.P.; Chen, Z.; Lu, H.; Waldeck, D.H. A Chemical Perspective on the Chiral Induced Spin Selectivity Effect. *Natl. Sci. Rev.* **2024**, *11*, nwae212, doi:10.1093/nsr/nwae212.
28. Evers, F.; Aharony, A.; Bar-Gill, N.; Entin-Wohlman, O.; Hedegård, P.; Hod, O.; Jelinek, P.; Kamieniarz, G.; Lemeshko, M.; Michaeli, K.; et al. Theory of Chirality Induced Spin Selectivity: Progress and Challenges. *Adv. Mater.* **2022**, *34*, 2106629, doi:10.1002/adma.202106629.

 doi:10.20944/preprints202603.2520.v1

29. Qi, D.; Kenaan, A.; Cui, D.; Song, J. Novel Insights into the Selection to Electron's Spin of Chiral Structure. *Nano Energy* **2018**, *52*, 142–152, doi:10.1016/j.nanoen.2018.07.054.
30. Fransson, J. The Chiral Induced Spin Selectivity Effect What It Is, What It Is Not, And Why It Matters. *Isr. J. Chem.* **2022**, *62*, e202200046, doi:10.1002/ijch.202200046.
31. Ghosh, S.; Banerjee-Ghosh, K.; Levy, D.; Scheerer, D.; Riven, I.; Shin, J.; Gray, H.B.; Naaman, R.; Haran, G. Control of Protein Activity by Photoinduced Spin Polarized Charge Reorganization. *Proc. Natl. Acad. Sci.* **2022**, *119*, e2204735119, doi:10.1073/pnas.2204735119.
32. Xu, Y.; Mi, W. Chiral-Induced Spin Selectivity in Biomolecules, Hybrid Organic–Inorganic Perovskites and Inorganic Materials: A Comprehensive Review on Recent Progress. *Mater. Horiz.* **2023**, *10*, 1924–1955, doi:10.1039/D3MH00024A.
33. Ma, S.; Lee, H.; Moon, J. Chirality-Induced Spin Selectivity Enables New Breakthrough in Electrochemical and Photoelectrochemical Reactions. *Adv. Mater.* **2024**, *36*, 2405685, doi:10.1002/adma.202405685.
34. Samokhvalov, A.; Berfeld, M.; Lahav, M.; Naaman, R.; Rabani, E. Assemblies of CdS Quantum Particles Studied by the Attenuated Low Energy Photoelectron Spectroscopy. *J. Phys. Chem. B* **2000**, *104*, 8631–8634, doi:10.1021/jp001709v.
35. Carmeli, I.; Gefen, Z.; Vager, Z.; Naaman, R. Alternation between Modes of Electron Transmission through Organized Organic Layers. *Phys. Rev. B* **2003**, *68*, 115418, doi:10.1103/PhysRevB.68.115418.
36. Ray, S.G.; Daube, S.S.; Leitus, G.; Vager, Z.; Naaman, R. Chirality-Induced Spin-Selective Properties of Self-Assembled Monolayers of DNA on Gold. *Phys. Rev. Lett.* **2006**, *96*, 036101, doi:10.1103/PhysRevLett.96.036101.
37. Carmeli, I.; Skakalova, V.; Naaman, R.; Vager, Z. Magnetization of Chiral Monolayers of Polypeptide: A Possible Source of Magnetism in Some Biological Membranes We Are Grateful to Prof. M. Fridkin and His Group for Helping Us in the Synthesis of the Polyalanine. Partial Support from the US–Israel Binational Science Foundation Is Acknowledged. *Angew. Chem. Int. Ed.* **2002**, *41*, 761, doi:10.1002/1521-3773(20020301)41:5%3C761::AID-ANIE761%3E3.0.CO;2-Z.
38. Rosenberg, R.A.; Abu Haija, M.; Ryan, P.J. Chiral-Selective Chemistry Induced by Spin-Polarized Secondary Electrons from a Magnetic Substrate. *Phys. Rev. Lett.* **2008**, *101*, 178301, doi:10.1103/PhysRevLett.101.178301.
39. Göhler, B.; Hamelbeck, V.; Markus, T.Z.; Kettner, M.; Hanne, G.F.; Vager, Z.; Naaman, R.; Zacharias, H. Spin Selectivity in Electron Transmission Through Self-Assembled Monolayers of Double-Stranded DNA. *Science* **2011**, *331*, 894–897, doi:10.1126/science.1199339.
40. Rosenberg, R.A.; Mishra, D.; Naaman, R. Chiral Selective Chemistry Induced by Natural Selection of Spin-Polarized Electrons. *Angew. Chem. Int. Ed.* **2015**, *54*, 7295–7298, doi:10.1002/anie.201501678.
41. Möllers, P.V.; Wei, J.; Salamon, S.; Bartsch, M.; Wende, H.; Waldeck, D.H.; Zacharias, H. Spin-Polarized Photoemission from Chiral CuO Catalyst Thin Films. *ACS Nano* **2022**, *16*, 12145–12155, doi:10.1021/acsnano.2c02709.
42. Xie, Z.; Markus, T.Z.; Cohen, S.R.; Vager, Z.; Gutierrez, R.; Naaman, R. Spin Specific Electron Conduction through DNA Oligomers. *Nano Lett.* **2011**, *11*, 4652–4655, doi:10.1021/nl2021637.
43. Hori, H.; Yamamoto, Y.; Iwamoto, T.; Miura, T.; Teranishi, T.; Miyake, M. Diameter Dependence of Ferromagnetic Spin Moment in Au Nanocrystals. *Phys. Rev. B* **2004**, *69*, 174411, doi:10.1103/PhysRevB.69.174411.
44. Nogues, C.; Cohen, S.R.; Daube, S.S.; Naaman, R. Electrical Properties of Short DNA Oligomers Characterized by Conducting Atomic Force Microscopy. *Phys. Chem. Chem. Phys.* **2004**, *6*, 4459, doi:10.1039/b410862k.
45. Albro, J.A.; Garrett, N.T.; Govindaraj, K.; Bloom, B.P.; Rosi, N.L.; Waldeck, D.H. Measurement Platform to Probe the Mechanism of Chiral-Induced Spin Selectivity through Direction-Dependent Magnetic Conductive Atomic Force Microscopy. *ACS Nano* **2025**, *19*, 17941–17949, doi:10.1021/acsnano.5c04980.
46. Sun, R.; Wang, Z.; Bloom, B.P.; Comstock, A.H.; Yang, C.; McConnell, A.; Clever, C.; Molitoris, M.; Lamont, D.; Cheng, Z.-H.; et al. Colossal Anisotropic Absorption of Spin Currents Induced by Chirality. *Sci. Adv.* **2024**, *10*, eadn3240, doi:10.1126/sciadv.adn3240.

 doi:10.20944/preprints202603.2520.v1

47. Labella, J.; Bhowmick, D.K.; Kumar, A.; Naaman, R.; Torres, T. Easily Processable Spin Filters: Exploring the Chiral Induced Spin Selectivity of Bowl-Shaped Chiral Subphthalocyanines. *Chem. Sci.* **2023**, *14*, 4273–4277, doi:10.1039/D3SC01069D.
48. Mishra, D.; Markus, T.Z.; Naaman, R.; Kettner, M.; Göhler, B.; Zacharias, H.; Friedman, N.; Sheves, M.; Fontanesi, C. Spin-Dependent Electron Transmission through Bacteriorhodopsin Embedded in Purple Membrane. *Proc. Natl. Acad. Sci.* **2013**, *110*, 14872–14876, doi:10.1073/pnas.1311493110.
49. Blumenschein, F.; Tamski, M.; Roussel, C.; Smolinsky, E.Z.B.; Tassinari, F.; Naaman, R.; Ansermet, J.-P. Spin-Dependent Charge Transfer at Chiral Electrodes Probed by Magnetic Resonance. *Phys. Chem. Chem. Phys.* **2020**, *22*, 997–1002, doi:10.1039/C9CP04681J.
50. Ferrari, C.; Bogdan, A.; Pop, F.; Curto, C.; Carella, A.; Rossella, F.; Avarvari, N.; Fontanesi, C. Enantio-Recognition and Charge Transfer Complex Formation Involving Tetrathiafulvalene-Appended Chiral 1,2-Cyclohexane-Diamine: An Integrated Experimental and Theoretical Study. *Chirality* **2024**, *36*, e70009, doi:10.1002/chir.70009.
51. Carella, A.; Mishra, S.; Ferrari, C.; Vanossi, D.; Rossella, F.; Pop, F.; Avarvari, N.; Htoon, H.; Hollingsworth, J.A.; Bowes, E.G.; et al. Chiral Induction at the Nanoscale and Spin Selectivity in Electron Transmission in Chiral Methylated BEDT-TTF Derivatives. *Nanoscale* **2025**, *17*, 2599–2607, doi:10.1039/D4NR04574B.
52. Grecchi, S.; Ferdeghini, C.; Longhi, M.; Mezzetta, A.; Guazzelli, L.; Khawthong, S.; Arduini, F.; Chiappe, C.; Iuliano, A.; Mussini, P.R. Chiral Biobased Ionic Liquids with Cations or Anions Including Bile Acid Building Blocks as Chiral Selectors in Voltammetry. *ChemElectroChem* **2021**, *8*, 1377–1387, doi:10.1002/celc.202100200.
53. Grecchi, S.; Arnaboldi, S.; Rizzo, S.; Mussini, P.R. Advanced Chiral Molecular Media for Enantioselective Electrochemistry and Electroanalysis. *Curr. Opin. Electrochem.* **2021**, *30*, 100810, doi:10.1016/j.coelec.2021.100810.
54. Rizzo, S.; Arnaboldi, S.; Mihali, V.; Cirilli, R.; Forni, A.; Gennaro, A.; Isse, A.A.; Pierini, M.; Mussini, P.R.; Sannicolò, F. "Inherently Chiral" Ionic-Liquid Media: Effective Chiral Electroanalysis on Achiral Electrodes. *Angew. Chem. Int. Ed.* **2017**, *56*, 2079–2082, doi:10.1002/anie.201607344.
55. Naaman, R.; Paltiel, Y.; Waldeck, D.H. Chirality and Spin: A Different Perspective on Enantioselective Interactions. *CHIMIA* **2018**, *72*, 394, doi:10.2533/chimia.2018.394.
56. Mishra, S.; Kumar, A.; Venkatesan, M.; Pigani, L.; Pasquali, L.; Fontanesi, C. Exchange Interactions Drive Supramolecular Chiral Induction in Polyaniline. *Small Methods* **2020**, *4*, 2000617, doi:10.1002/smtd.202000617.
57. Mishra, S.; Pasquali, L.; Fontanesi, C. Spin Control Using Chiral Templated Nickel. *Appl. Phys. Lett.* **2021**, *118*, 224001, doi:10.1063/5.0049113.
58. Naaman, R.; Paltiel, Y.; Waldeck, D.H. Chiral Molecules and the Spin Selectivity Effect. *J. Phys. Chem. Lett.* **2020**, *11*, 3660–3666, doi:10.1021/acs.jpclett.0c00474.
59. Stefani, A.; Salzillo, T.; Mussini, P.R.; Benincori, T.; Innocenti, M.; Pasquali, L.; Jones, A.C.; Mishra, S.; Fontanesi, C. Chiral Recognition: A Spin-Driven Process in Chiral Oligothiophene. A Chiral-Induced Spin Selectivity (CISS) Effect Manifestation. *Adv. Funct. Mater.* **2024**, *34*, 2308948, doi:10.1002/adfm.202308948.
60. Mondal, P.C.; Fontanesi, C.; Waldeck, D.H.; Naaman, R. Field and Chirality Effects on Electrochemical Charge Transfer Rates: Spin Dependent Electrochemistry. *ACS Nano* **2015**, *9*, 3377–3384, doi:10.1021/acsnano.5b00832.
61. Chiesa, A.; Privitera, A.; Macaluso, E.; Mannini, M.; Bittl, R.; Naaman, R.; Wasielewski, M.R.; Sessoli, R.; Carretta, S. Chirality-Induced Spin Selectivity: An Enabling Technology for Quantum Applications. *Adv. Mater.* **2023**, *35*, 2300472, doi:10.1002/adma.202300472.
62. Mishra, S.; Jones, A.C.; Fontanesi, C. Recent Advancements in Chiral Spintronics: From Molecular-Level Insights to Device Applications. A Prospect Based on the Interplay between Physical and Chemical Properties of Chiral Systems. *J. Mater. Chem. C* **2025**, *13*, 2121–2134, doi:10.1039/D4TC03453H.
63. Aizawa, H.; Sato, T.; Maki-Yonekura, S.; Yonekura, K.; Takaba, K.; Hamaguchi, T.; Minato, T.; Yamamoto, H.M. Enantioselectivity of Discretized Helical Supramolecule Consisting of Achiral Cobalt Phthalocyanines via Chiral-Induced Spin Selectivity Effect. *Nat. Commun.* **2023**, *14*, 4530, doi:10.1038/s41467-023-40133-z.

 doi:10.20944/preprints202603.2520.v1

64. Ko, C.-H.; Zhu, Q.; Bullard, G.; Tassinari, F.; Morisue, M.; Naaman, R.; Therien, M.J. Electron Spin Polarization and Rectification Driven by Chiral Perylene Diimide-Based Nanodonuts. *J. Phys. Chem. Lett.* **2023**, *14*, 10271–10277, doi:10.1021/acs.jpclett.3c02722.
65. Gersten, J.; Kaasbjerg, K.; Nitzan, A. Induced Spin Filtering in Electron Transmission through Chiral Molecular Layers Adsorbed on Metals with Strong Spin-Orbit Coupling. *J. Chem. Phys.* **2013**, *139*, 114111, doi:10.1063/1.4820907.
66. Liu, Y.; Xiao, J.; Koo, J.; Yan, B. Chirality-Driven Topological Electronic Structure of DNA-like Materials. *Nat. Mater.* **2021**, *20*, 638–644, doi:10.1038/s41563-021-00924-5.
67. Dubi, Y. Spinterface Chirality-Induced Spin Selectivity Effect in Bio-Molecules. *Chem. Sci.* **2022**, *13*, 10878–10883, doi:10.1039/D2SC02565E.
68. Stephens, P.J. Magnetic Circular Dichroism. *Annu. Rev. Phys. Chem.* **1974**, *25*, 201–232, doi:10.1146/annurev.pc.25.100174.001221.
69. Varela, S.; Gutierrez, R.; Cuniberti, G.; Medina, E.; Mujica, V. Electron Spin Polarization as a Predictor of Chiroptical Activity in Helical Molecules 2023.
70. Fay, T.P. Chirality-Induced Spin Coherence in Electron Transfer Reactions. *J. Phys. Chem. Lett.* **2021**, *12*, 1407–1412, doi:10.1021/acs.jpclett.1c00009.
71. Mishra, S.; Bowes, E.G.; Majumder, S.; Hollingsworth, J.A.; Htoon, H.; Jones, A.C. Inducing Circularly Polarized Single-Photon Emission via Chiral-Induced Spin Selectivity. *ACS Nano* **2024**, *18*, 8663–8672, doi:10.1021/acsnano.3c08676.
72. Roy, P.; Kantor-Uriel, N.; Mishra, D.; Dutta, S.; Friedman, N.; Sheves, M.; Naaman, R. Spin-Controlled Photoluminescence in Hybrid Nanoparticles Purple Membrane System. *ACS Nano* **2016**, *10*, 4525–4531, doi:10.1021/acsnano.6b00333.
73. Bloom, B.P.; Graff, B.M.; Ghosh, S.; Beratan, D.N.; Waldeck, D.H. Chirality Control of Electron Transfer in Quantum Dot Assemblies. *J. Am. Chem. Soc.* **2017**, *139*, 9038–9043, doi:10.1021/jacs.7b04639.
74. Mondal, P.C.; Roy, P.; Kim, D.; Fullerton, E.E.; Cohen, H.; Naaman, R. Photospintronics: Magnetic Field-Controlled Photoemission and Light-Controlled Spin Transport in Hybrid Chiral Oligopeptide-Nanoparticle Structures. *Nano Lett.* **2016**, *16*, 2806–2811, doi:10.1021/acs.nanolett.6b00582.
75. Sherson, J.F.; Krauter, H.; Olsson, R.K.; Julsgaard, B.; Hammerer, K.; Cirac, I.; Polzik, E.S. Quantum Teleportation between Light and Matter. *Nature* **2006**, *443*, 557–560, doi:10.1038/nature05136.
76. Farshchi, R.; Ramsteiner, M.; Herfort, J.; Tahraoui, A.; Grahn, H.T. Optical Communication of Spin Information between Light Emitting Diodes. *Appl. Phys. Lett.* **2011**, *98*, 162508, doi:10.1063/1.3582917.
77. Yang, Y.; Da Costa, R.C.; Fuchter, M.J.; Campbell, A.J. Circularly Polarized Light Detection by a Chiral Organic Semiconductor Transistor. *Nat. Photonics* **2013**, *7*, 634–638, doi:10.1038/nphoton.2013.176.
78. Han, H.; Lee, Y.J.; Kyhm, J.; Jeong, J.S.; Han, J.; Yang, M.K.; Lee, K.M.; Choi, Y.; Yoon, T.; Ju, H.; et al. High-Performance Circularly Polarized Light-Sensing Near-Infrared Organic Phototransistors for Optoelectronic Cryptographic Primitives. *Adv. Funct. Mater.* **2020**, *30*, 2006236, doi:10.1002/adfm.202006236.
79. Gu, H.; Xia, J.; Liang, C.; Chen, Y.; Huang, W.; Xing, G. Phase-Pure Two-Dimensional Layered Perovskite Thin Films. *Nat. Rev. Mater.* **2023**, *8*, 533–551, doi:10.1038/s41578-023-00560-2.
80. Sidhik, S.; Wang, Y.; Li, W.; Zhang, H.; Zhong, X.; Agrawal, A.; Hadar, I.; Spanopoulos, I.; Mishra, A.; Traoré, B.; et al. High-Phase Purity Two-Dimensional Perovskites with 17.3% Efficiency Enabled by Interface Engineering of Hole Transport Layer. *Cell Rep. Phys. Sci.* **2021**, *2*, 100601, doi:10.1016/j.xcrp.2021.100601.
81. Lu, H.; Wang, J.; Xiao, C.; Pan, X.; Chen, X.; Brunecky, R.; Berry, J.J.; Zhu, K.; Beard, M.C.; Vardeny, Z.V. Spin-Dependent Charge Transport through 2D Chiral Hybrid Lead-Iodide Perovskites. *Sci. Adv.* **2019**, *5*, eaay0571, doi:10.1126/sciadv.aay0571.
82. Lu, H.; Xiao, C.; Song, R.; Li, T.; Maughan, A.E.; Levin, A.; Brunecky, R.; Berry, J.J.; Mitzi, D.B.; Blum, V.; et al. Highly Distorted Chiral Two-Dimensional Tin Iodide Perovskites for Spin Polarized Charge Transport. *J. Am. Chem. Soc.* **2020**, *142*, 13030–13040, doi:10.1021/jacs.0c03899.
83. *Organic Spintronics*; Vardeny, Z.V., Ed.; 1st edition.; CRC Press: Boca Raton, 2017; ISBN 978-1-4398-0657-9.

 doi:10.20944/preprints202603.2520.v1

84. Firouzeh, S.; Hossain, M.A.; Cuerva, J.M.; Álvarez De Cienfuegos, L.; Pramanik, S. Chirality-Induced Spin Selectivity in Composite Materials: A Device Perspective. *Acc. Chem. Res.* **2024**, *57*, 1478–1487, doi:10.1021/acs.accounts.4c00077.
85. Mishra, S.; Mondal, A.K.; Smolinsky, E.Z.B.; Naaman, R.; Maeda, K.; Nishimura, T.; Taniguchi, T.; Yoshida, T.; Takayama, K.; Yashima, E. Spin Filtering Along Chiral Polymers. *Angew. Chem. Int. Ed.* **2020**, *59*, 14671–14676, doi:10.1002/anie.202006570.
86. Kondou, K.; Shiga, M.; Sakamoto, S.; Inuzuka, H.; Nihonyanagi, A.; Araoka, F.; Kobayashi, M.; Miwa, S.; Miyajima, D.; Otani, Y. Chirality-Induced Magnetoresistance Due to Thermally Driven Spin Polarization. *J. Am. Chem. Soc.* **2022**, *144*, 7302–7307, doi:10.1021/jacs.2c00496.
87. Ohe, K.; Shishido, H.; Kato, M.; Utsumi, S.; Matsuura, H.; Togawa, Y. Chirality-Induced Selectivity of Phonon Angular Momenta in Chiral Quartz Crystals. *Phys. Rev. Lett.* **2024**, *132*, 056302, doi:10.1103/PhysRevLett.132.056302.
88. Gust, D.; Moore, T.A.; Moore, A.L. Solar Fuels via Artificial Photosynthesis. *Acc. Chem. Res.* **2009**, *42*, 1890–1898, doi:10.1021/ar900209b.
89. Mtangi, W.; Kiran, V.; Fontanesi, C.; Naaman, R. Role of the Electron Spin Polarization in Water Splitting. *J. Phys. Chem. Lett.* **2015**, *6*, 4916–4922, doi:10.1021/acs.jpclett.5b02419.
90. Barik, D.; Utkarsh, U.; Ghosh, K.B. Spin-Controlled Electrocatalysis: An out-of-the-Box Strategy for the Advancement of Electrochemical Water Splitting. *Chem. Commun.* **2025**, *61*, 6226–6245, doi:10.1039/D5CC01305D.
91. Lin, L.; Su, P.; Han, Y.; Xu, Y.; Ni, Q.; Zhang, X.; Xiong, P.; Sun, Z.; Sun, G.; Chen, X. Advances in Regulating the Electron Spin Effect toward Electrocatalysis Applications. *eScience* **2025**, *5*, 100264, doi:10.1016/j.esci.2024.100264.
92. Nair, A.N.; Fernandez, S.; Marcos-Hernández, M.; Romo, D.R.; Singamaneni, S.R.; Villagran, D.; Sreenivasan, S.T. Spin-Selective Oxygen Evolution Reaction in Chiral Iron Oxide Nanoparticles: Synergistic Impact of Inherent Magnetic Moment and Chirality. *Nano Lett.* **2023**, *23*, 9042–9049, doi:10.1021/acs.nanolett.3c02752.
93. Wang, Z.; Wan, J.; Sun, X.; Sun, L.; Chen, S.; Zhang, Q. Boosting the Selectivity in Oxygen Electrocatalysis Using Chiral Nanoparticles as Electron-Spin Filters. *J. Am. Chem. Soc.* **2025**, *147*, 15767–15776, doi:10.1021/jacs.5c03394.
94. Liang, Y.; Banjac, K.; Martin, K.; Zigon, N.; Lee, S.; Vanthuyne, N.; Garcés-Pineda, F.A.; Galán-Mascarós, J.R.; Hu, X.; Avarvari, N.; et al. Enhancement of Electrocatalytic Oxygen Evolution by Chiral Molecular Functionalization of Hybrid 2D Electrodes. *Nat. Commun.* **2022**, *13*, 3356, doi:10.1038/s41467-022-31096-8.
95. Rai, S.; Prachi, P.; Kant, C.R.; Jha, R. Metal-Air Batteries: From Fundamental Mechanisms to Practical Applications. *J. Alloys Compd.* **2025**, *1033*, 180805, doi:10.1016/j.jallcom.2025.180805.
96. Wang, C.; Yu, Y.; Niu, J.; Liu, Y.; Bridges, D.; Liu, X.; Pooran, J.; Zhang, Y.; Hu, A. Recent Progress of Metal–Air Batteries—A Mini Review. *Appl. Sci.* **2019**, *9*, 2787, doi:10.3390/app9142787.
97. Pellow, M.A.; Emmott, C.J.M.; Barnhart, C.J.; Benson, S.M. Hydrogen or Batteries for Grid Storage? A Net Energy Analysis. *Energy Environ. Sci.* **2015**, *8*, 1938–1952, doi:10.1039/C4EE04041D.
98. Jeżowski, P.; Fic, K.; Crosnier, O.; Brousse, T.; Béguin, F. Use of Sacrificial Lithium Nickel Oxide for Loading Graphitic Anode in Li-Ion Capacitors. *Electrochimica Acta* **2016**, *206*, 440–445, doi:10.1016/j.electacta.2015.12.034.
99. Abraham, K.M.; Jiang, Z. A Polymer Electrolyte-Based Rechargeable Lithium/Oxygen Battery. *J. Electrochem. Soc.* **1996**, *143*, 1–5, doi:10.1149/1.1836378.
100. Zhang, X. *Metal-Air Batteries: Fundamentals and Applications*; Wiley-VCH: Weinheim, 2018; ISBN 978-3-527-34279-2.
101. Zhang, X.; Wang, X.-G.; Xie, Z.; Zhou, Z. Recent Progress in Rechargeable Alkali Metal–Air Batteries. *Green Energy Environ.* **2016**, *1*, 4–17, doi:10.1016/j.gee.2016.04.004.
102. Durmus, Y.E.; Zhang, H.; Baakes, F.; Desmaizieres, G.; Hayun, H.; Yang, L.; Kolek, M.; Küpers, V.; Janek, J.; Mandler, D.; et al. Side by Side Battery Technologies with Lithium-Ion Based Batteries. *Adv. Energy Mater.* **2020**, *10*, 2000089, doi:10.1002/aenm.202000089.

 doi:10.20944/preprints202603.2520.v1

103. Liu, Q.; Chang, Z.; Li, Z.; Zhang, X. Flexible Metal–Air Batteries: Progress, Challenges, and Perspectives. *Small Methods* **2018**, *2*, 1700231, doi:10.1002/smtd.201700231.
104. Wang, Y.; Kwok, H.; Pan, W.; Zhang, H.; Leung, D.Y.C. Innovative Paper-Based Al-Air Batteries as a Low-Cost and Green Energy Technology for the Miniwatt Market. *J. Power Sources* **2019**, *414*, 278–282, doi:10.1016/j.jpowsour.2019.01.018.
105. Wu, D.; Guo, Z.; Yin, X.; Pang, Q.; Tu, B.; Zhang, L.; Wang, Y.; Li, Q. Metal–Organic Frameworks as Cathode Materials for Li–O_2 Batteries. *Adv. Mater.* **2014**, *26*, 3258–3262, doi:10.1002/adma.201305492.
106. Cheng, F.; Chen, J. Metal–Air Batteries: From Oxygen Reduction Electrochemistry to Cathode Catalysts. *Chem. Soc. Rev.* **2012**, *41*, 2172, doi:10.1039/c1cs15228a.
107. Zhang, L.; Cheng, J.; Yang, Y.; Wen, Y.; Wang, X.; Xie, Z. Preliminary Study of Single Flow Zinc-Nickel Battery. *J. Electrochem.* **2008**, *14*, doi:10.61558/2993-074X.1900.
108. Fu, J.; Zhang, J.; Song, X.; Zarrin, H.; Tian, X.; Qiao, J.; Rasen, L.; Li, K.; Chen, Z. A Flexible Solid-State Electrolyte for Wide-Scale Integration of Rechargeable Zinc–Air Batteries. *Energy Environ. Sci.* **2016**, *9*, 663–670, doi:10.1039/C5EE03404C.
109. Zhou, G.; Li, F.; Cheng, H.-M. Progress in Flexible Lithium Batteries and Future Prospects. *Energy Env. Sci* **2014**, *7*, 1307–1338, doi:10.1039/C3EE43182G.
110. Sumboja, A.; Ge, X.; Zong, Y.; Liu, Z. Progress in Development of Flexible Metal–Air Batteries. *Funct. Mater. Lett.* **2016**, *09*, 1630001, doi:10.1142/S1793604716300012.
111. Pan, J.; Xu, Y.Y.; Yang, H.; Dong, Z.; Liu, H.; Xia, B.Y. Advanced Architectures and Relatives of Air Electrodes in Zn–Air Batteries. *Adv. Sci.* **2018**, *5*, 1700691, doi:10.1002/advs.201700691.
112. Li, Y.; Lu, J. Metal–Air Batteries: Will They Be the Future Electrochemical Energy Storage Device of Choice? *ACS Energy Lett.* **2017**, *2*, 1370–1377, doi:10.1021/acsenergylett.7b00119.
113. Yaqoob, L.; Noor, T.; Iqbal, N. An Overview of Metal-Air Batteries, Current Progress, and Future Perspectives. *J. Energy Storage* **2022**, *56*, 106075, doi:10.1016/j.est.2022.106075.
114. Asmare, M.; Zegeye, M.; Ketema, A. Advancement of Electrically Rechargeable Metal-Air Batteries for Future Mobility. *Energy Rep.* **2024**, *11*, 1199–1211, doi:10.1016/j.egyr.2023.12.067.
115. Mao, P.; Arandiyan, H.; Mofarah, S.S.; Koshy, P.; Pozo-Gonzalo, C.; Zheng, R.; Wang, Z.; Wang, Y.; Bhargava, S.K.; Sun, H.; et al. A Comprehensive Review of Cathode Materials for Na–Air Batteries. *Energy Adv.* **2023**, *2*, 465–502, doi:10.1039/D2YA00340F.
116. Kraytsberg, A.; Ein-Eli, Y. Review on Li–Air Batteries—Opportunities, Limitations and Perspective. *J. Power Sources* **2011**, *196*, 886–893, doi:10.1016/j.jpowsour.2010.09.031.
117. Imanishi, N.; Matsui, M.; Takeda, Y.; Yamamoto, O. Lithium Ion Conducting Solid Electrolytes for Aqueous Lithium-Air Batteries. *Electrochemistry* **2014**, *82*, 938–945, doi:10.5796/electrochemistry.82.938.
118. Lu, Y.-C.; Xu, Z.; Gasteiger, H.A.; Chen, S.; Hamad-Schifferli, K.; Shao-Horn, Y. Platinum−Gold Nanoparticles: A Highly Active Bifunctional Electrocatalyst for Rechargeable Lithium−Air Batteries. *J. Am. Chem. Soc.* **2010**, *132*, 12170–12171, doi:10.1021/ja1036572.
119. Yang, S. Design and Analysis of Aluminum/Air Battery System for Electric Vehicles. *J. Power Sources* **2002**, *112*, 162–173, doi:10.1016/S0378-7753(02)00370-1.
120. Rani, B.; Yadav, J.K.; Saini, P.; Pandey, A.P.; Dixit, A. Aluminum–Air Batteries: Current Advances and Promises with Future Directions. *RSC Adv.* **2024**, *14*, 17628–17663, doi:10.1039/D4RA02219J.
121. Fan, L.; Lu, H. The Effect of Grain Size on Aluminum Anodes for Al–Air Batteries in Alkaline Electrolytes. *J. Power Sources* **2015**, *284*, 409–415, doi:10.1016/j.jpowsour.2015.03.063.
122. Inoishi, A.; Sakai, T.; Ju, Y.W.; Ida, S.; Ishihara, T. Improved Cycle Stability of Fe–Air Solid State Oxide Rechargeable Battery Using LaGaO3-Based Oxide Ion Conductor. *J. Power Sources* **2014**, *262*, 310–315, doi:10.1016/j.jpowsour.2014.03.125.
123. Sun, X.; Li, H.; Song, Y.; Liu, J.; Ji, P.; Lei, X.; Zhang, X.; Liu, Q.; Li, M.; Deng, B.; et al. Cascade Reactors for Long-Life Solid-State Sodium–Air Batteries. *Nat. Commun.* **2025**, *16*, 5814, doi:10.1038/s41467-025-60840-z.
124. Goel, P.; Dobhal, D.; Sharma, R.C. Aluminum–Air Batteries: A Viability Review. *J. Energy Storage* **2020**, *28*, 101287, doi:10.1016/j.est.2020.101287.

 doi:10.20944/preprints202603.2520.v1

125. Villanueva, N.; Alegre, C.; Rubin, J.; Figueredo-Rodríguez, H.A.; McKerracher, R.D.; De León, C.P.; Lázaro, M.J. Iron Electrodes Based on Sulfur-Modified Iron Oxides with Enhanced Stability for Iron–Air Batteries. *ACS Appl. Energy Mater.* **2022**, *5*, 13439–13451, doi:10.1021/acsaem.2c02123.
126. Betz, J.; Bieker, G.; Meister, P.; Placke, T.; Winter, M.; Schmuch, R. Theoretical versus Practical Energy: A Plea for More Transparency in the Energy Calculation of Different Rechargeable Battery Systems. *Adv. Energy Mater.* **2019**, *9*, 1803170, doi:10.1002/aenm.201803170.
127. Schmuch, R.; Wagner, R.; Hörpel, G.; Placke, T.; Winter, M. Performance and Cost of Materials for Lithium-Based Rechargeable Automotive Batteries. *Nat. Energy* **2018**, *3*, 267–278, doi:10.1038/s41560-018-0107-2.
128. Clark, S.; Latz, A.; Horstmann, B. A Review of Model-Based Design Tools for Metal-Air Batteries. *Batteries* **2018**, *4*, 5, doi:10.3390/batteries4010005.
129. Jin, S.; Hong, S.; Archer, L.A. Self-Sufficient Metal–Air Batteries for Autonomous Systems. *Nat. Chem. Eng.* **2024**, *1*, 194–197, doi:10.1038/s44286-024-00039-z.
130. Greszler, T.; Gu, W.; Goebel, S.; Masten, D.; Lakshmanan, B. Li Air and Li-Sulfur in an Automotive System Context.; Berkeley, CA USA, June 2012.
131. Placke, T.; Kloepsch, R.; Dühnen, S.; Winter, M. Lithium Ion, Lithium Metal, and Alternative Rechargeable Battery Technologies: The Odyssey for High Energy Density. *J. Solid State Electrochem.* **2017**, *21*, 1939–1964, doi:10.1007/s10008-017-3610-7.
132. Hardwick, L.J.; De León, C.P. Rechargeable Multi-Valent Metal-Air Batteries: A Review of Research and Current Challenges in Secondary Multivalent Metal-Oxygen Batteries. *Johns. Matthey Technol. Rev.* **2018**, *62*, 134–149, doi:10.1595/205651318X696729.
133. Zhang, H.; Chen, H.; Feizpoor, S.; Li, L.; Zhang, X.; Xu, X.; Zhuang, Z.; Li, Z.; Hu, W.; Snyders, R.; et al. Tailoring Oxygen Reduction Reaction Kinetics of Fe−N−C Catalyst via Spin Manipulation for Efficient Zinc–Air Batteries. *Adv. Mater.* **2024**, *36*, 2400523, doi:10.1002/adma.202400523.
134. Cao, D.; Zhang, S.; Yu, F.; Wu, Y.; Chen, Y. Carbon-Free Cathode Materials for Li−O_2 Batteries. *Batter. Supercaps* **2019**, *2*, 428–439, doi:10.1002/batt.201800133.
135. Ling, C.; Zhang, R.; Takechi, K.; Mizuno, F. Intrinsic Barrier to Electrochemically Decompose Li_2CO_3 and LiOH. *J. Phys. Chem. C* **2014**, *118*, 26591–26598, doi:10.1021/jp5093306.
136. Li, F.; Wu, S.; Li, D.; Zhang, T.; He, P.; Yamada, A.; Zhou, H. The Water Catalysis at Oxygen Cathodes of Lithium–Oxygen Cells. *Nat. Commun.* **2015**, *6*, 7843, doi:10.1038/ncomms8843.
137. Abendroth, J.M.; Stemer, D.M.; Bloom, B.P.; Roy, P.; Naaman, R.; Waldeck, D.H.; Weiss, P.S.; Mondal, P.C. Spin Selectivity in Photoinduced Charge-Transfer Mediated by Chiral Molecules. *ACS Nano* **2019**, *13*, 4928–4946, doi:10.1021/acsnano.9b01876.
138. Mtangi, W.; Tassinari, F.; Vankayala, K.; Vargas Jentzsch, A.; Adelizzi, B.; Palmans, A.R.A.; Fontanesi, C.; Meijer, E.W.; Naaman, R. Control of Electrons' Spin Eliminates Hydrogen Peroxide Formation During Water Splitting. *J. Am. Chem. Soc.* **2017**, *139*, 2794–2798, doi:10.1021/jacs.6b12971.
139. Vadakkayil, A.; Dunlap-Shohl, W.A.; Joy, M.; Bloom, B.P.; Waldeck, D.H. Improved Catalyst Performance for the Oxygen Evolution Reaction under a Chiral Bias. *ACS Catal.* **2024**, *14*, 17303–17309, doi:10.1021/acscatal.4c04477.
140. Bruce, P.G.; Freunberger, S.A.; Hardwick, L.J.; Tarascon, J.-M. Li–O2 and Li–S Batteries with High Energy Storage. *Nat. Mater.* **2012**, *11*, 19–29, doi:10.1038/nmat3191.
141. Ghosh, K.B.; Zhang, W.; Tassinari, F.; Mastai, Y.; Lidor-Shalev, O.; Naaman, R.; Möllers, P.; Nürenberg, D.; Zacharias, H.; Wei, J.; et al. Controlling Chemical Selectivity in Electrocatalysis with Chiral CuO-Coated Electrodes. *J. Phys. Chem. C* **2019**, *123*, 3024–3031, doi:10.1021/acs.jpcc.8b12027.
142. Liu, X.; Yuan, Y.; Liu, J.; Liu, B.; Chen, X.; Ding, J.; Han, X.; Deng, Y.; Zhong, C.; Hu, W. Utilizing Solar Energy to Improve the Oxygen Evolution Reaction Kinetics in Zinc–Air Battery. *Nat. Commun.* **2019**, *10*, 4767, doi:10.1038/s41467-019-12627-2.
143. Noor, T.; Yaqoob, L.; Iqbal, N. Recent Advances in Electrocatalysis of Oxygen Evolution Reaction Using Noble-Metal, Transition-Metal, and Carbon-Based Materials. *ChemElectroChem* **2021**, *8*, 447–483, doi:10.1002/celc.202001441.

 doi:10.20944/preprints202603.2520.v1

144. Li, Z.; Xiao, Y.; Jiang, C.; Hou, B.; Liu, Y.; Cui, Y. Engineering Spin-Dependent Catalysts: Chiral Covalent Organic Frameworks with Tunable Electroactivity for Electrochemical Oxygen Evolution. *Natl. Sci. Rev.* **2024**, *11*, nwae332, doi:10.1093/nsr/nwae332.
145. Singh, A.-K.; Martin, K.; Mastropasqua Talamo, M.; Houssin, A.; Vanthuyne, N.; Avarvari, N.; Tal, O. Single-Molecule Junctions Map the Interplay between Electrons and Chirality. *Nat. Commun.* **2025**, *16*, 1759, doi:10.1038/s41467-025-56718-9.
146. Krieger, J.A.; Stolz, S.; Robredo, I.; Manna, K.; McFarlane, E.C.; Date, M.; Pal, B.; Yang, J.; B. Guedes, E.; Dil, J.H.; et al. Weyl Spin-Momentum Locking in a Chiral Topological Semimetal. *Nat. Commun.* **2024**, *15*, 3720, doi:10.1038/s41467-024-47976-0.
147. Mtangi, W.; Kiran, V.; Fontanesi, C.; Naaman, R. Role of the Electron Spin Polarization in Water Splitting. *J. Phys. Chem. Lett.* **2015**, *6*, 4916–4922, doi:10.1021/acs.jpclett.5b02419.
148. Naaman, R.; Fontanesi, C.; Mtangi, W. Water Splitting Method and System 2016, 39.
149. Wang, D.; Pan, X.; Yang, P.; Li, R.; Xu, H.; Li, Y.; Meng, F.; Zhang, J.; An, M. Transition Metal and Nitrogen Co-Doped Carbon-based Electrocatalysts for the Oxygen Reduction Reaction: From Active Site Insights to the Rational Design of Precursors and Structures. *ChemSusChem* **2021**, *14*, 33–55, doi:10.1002/cssc.202002137.
150. Rufino Júnior, C.A.; Sanseverino, E.R.; Gallo, P.; Amaral, M.M.; Koch, D.; Kotak, Y.; Diel, S.; Walter, G.; Schweiger, H.-G.; Zanin, H. Unraveling the Degradation Mechanisms of Lithium-Ion Batteries. *Energies* **2024**, *17*, 3372, doi:10.3390/en17143372.
151. Kim, J.H.; Kim, Y.-T.; Joo, S.H. Electrocatalyst Design for Promoting Two-Electron Oxygen Reduction Reaction: Isolation of Active Site Atoms. *Curr. Opin. Electrochem.* **2020**, *21*, 109–116, doi:10.1016/j.coelec.2020.01.007.
152. Liu, J.; Zhou, M.; Jin, K.; Li, J.; Meng, F.; Wei, X. Beyond Metal–Air Battery, Emerging Aqueous Metal–Hydrogen Peroxide Batteries with Improved Performance. *Battery Energy* **2024**, *3*, 20230049, doi:10.1002/bte2.20230049.
153. Yu, A.; Yang, Y. Atomically Dispersed Metal Catalysts for Oxygen Reduction Reaction: Two-Electron vs. Four-Electron Pathways. *Angew. Chem.* **2025**, *137*, e202424161, doi:10.1002/ange.202424161.
154. Scarpetta-Pizo, L.; Venegas, R.; Barrías, P.; Muñoz-Becerra, K.; Vilches-Labbé, N.; Mura, F.; Méndez-Torres, A.M.; Ramírez-Tagle, R.; Toro-Labbé, A.; Hevia, S.; et al. Electron Spin-Dependent Electrocatalysis for the Oxygen Reduction Reaction in a Chiro-Self-Assembled Iron Phthalocyanine Device. *Angew. Chem. Int. Ed.* **2024**, *63*, e202315146, doi:10.1002/anie.202315146.
155. Xia, Q.; Zhai, Y.; Zhao, L.; Wang, J.; Li, D.; Zhang, L.; Zhang, J. Carbon-Supported Single-Atom Catalysts for Advanced Rechargeable Metal-Air Batteries. *Energy Mater.* **2022**, *2*, doi:10.20517/energymater.2022.13.
156. Ma, R.; Lin, G.; Zhou, Y.; Liu, Q.; Zhang, T.; Shan, G.; Yang, M.; Wang, J. A Review of Oxygen Reduction Mechanisms for Metal-Free Carbon-Based Electrocatalysts. *Npj Comput. Mater.* **2019**, *5*, 78, doi:10.1038/s41524-019-0210-3.
157. Vadakkayil, A.; Clever, C.; Kunzler, K.N.; Tan, S.; Bloom, B.P.; Waldeck, D.H. Chiral Electrocatalysts Eclipse Water Splitting Metrics through Spin Control. *Nat. Commun.* **2023**, *14*, 1067, doi:10.1038/s41467-023-36703-w.
158. Shi, X.-D.; Guo, R.; Cui, H.; Liu, C.; Pan, W. Electrocatalytic Reduction of CO_2 to Produce the C_{2+} Products: From Selectivity to Rational Catalyst Design. *Nanoscale* **2025**, *17*, 4338–4364, doi:10.1039/D4NR04159C.
159. Nitopi, S.; Bertheussen, E.; Scott, S.B.; Liu, X.; Engstfeld, A.K.; Horch, S.; Seger, B.; Stephens, I.E.L.; Chan, K.; Hahn, C.; et al. Progress and Perspectives of Electrochemical CO_2 Reduction on Copper in Aqueous Electrolyte. *Chem. Rev.* **2019**, *119*, 7610–7672, doi:10.1021/acs.chemrev.8b00705.
160. Kumar De, S.; Won, D.-I.; Kim, J.; Kim, D.H. Integrated CO_2 Capture and Electrochemical Upgradation: The Underpinning Mechanism and Techno-Chemical Analysis. *Chem. Soc. Rev.* **2023**, *52*, 5744–5802, doi:10.1039/D2CS00512C.
161. Chen, Z.; Li, X.; Ma, H.; Zhang, Y.; Peng, J.; Ma, T.; Cheng, Z.; Gracia, J.; Sun, Y.; Xu, Z.J. Spin-Dependent Electrocatalysis. *Natl. Sci. Rev.* **2024**, *11*, nwae314, doi:10.1093/nsr/nwae314.
162. Zhao, J.; Lin, S. Towards Superior CO2RR Catalysts: Deciphering the Selectivity Puzzle over Dual-Atom Catalyst. *J. Colloid Interface Sci.* **2025**, *680*, 257–264, doi:10.1016/j.jcis.2024.11.080.

 doi:10.20944/preprints202603.2520.v1

163. Yan, X.; Li, J.; Si, H.; Xu, H.; Huang, H.; Liu, Y.; Kang, Z. Multifunctions of Carbon Dots in the CeO_2 /Cu_2 O Complex Catalyst for the Regulation of Carbon Dioxide Reduction. *Inorg. Chem. Front.* **2025**, *12*, 2024–2035, doi:10.1039/D4QI02744B.
164. Marcandalli, G.; Monteiro, M.C.O.; Goyal, A.; Koper, M.T.M. Electrolyte Effects on CO_2 Electrochemical Reduction to CO. *Acc. Chem. Res.* **2022**, *55*, 1900–1911, doi:10.1021/acs.accounts.2c00080.
165. Varela, A.S. Effect of the Reaction Environment on the CO2 Electrochemical Reduction. *Chem Catal.* **2022**, *2*, 233–235, doi:10.1016/j.checat.2022.01.009.
166. Suntivich, J.; Gasteiger, H.A.; Yabuuchi, N.; Nakanishi, H.; Goodenough, J.B.; Shao-Horn, Y. Design Principles for Oxygen-Reduction Activity on Perovskite Oxide Catalysts for Fuel Cells and Metal–Air Batteries. *Nat. Chem.* **2011**, *3*, 546–550, doi:10.1038/nchem.1069.
167. Li, S.; Liu, J.; Yin, Z.; Ren, P.; Lin, L.; Gong, Y.; Yang, C.; Zheng, X.; Cao, R.; Yao, S.; et al. Impact of the Coordination Environment on Atomically Dispersed Pt Catalysts for Oxygen Reduction Reaction. *ACS Catal.* **2020**, *10*, 907–913, doi:10.1021/acscatal.9b04558.
168. Zhang, Y.; Liang, C.; Wu, J.; Liu, H.; Zhang, B.; Jiang, Z.; Li, S.; Xu, P. Recent Advances in Magnetic Field-Enhanced Electrocatalysis. *ACS Appl. Energy Mater.* **2020**, *3*, 10303–10316, doi:10.1021/acsaem.0c02104.
169. Pan, H.; Jiang, X.; Wang, X.; Wang, Q.; Wang, M.; Shen, Y. Effective Magnetic Field Regulation of the Radical Pair Spin States in Electrocatalytic CO_2 Reduction. *J. Phys. Chem. Lett.* **2020**, *11*, 48–53, doi:10.1021/acs.jpclett.9b03146.
170. Nankya, R.; Wang, H. Chiral Cu Surfaces for Efficient Amino Acid Synthesis via CO2 Electrolysis. *Chem Catal.* **2023**, *3*, 100510, doi:10.1016/j.checat.2023.100510.
171. Yousaf, S.; Ahmad, I.; Farooq Warsi, M.; Ali, A. Engineering Strategies in the Rational Design of Cu-Based Catalysts for Electrochemical CO_2 Reduction: From Doping of Elements to Defect Creation. *Mater. Adv.* **2024**, *5*, 7891–7978, doi:10.1039/D4MA00321G.
172. Fang, Y.; Liu, X.; Liu, Z.; Han, L.; Ai, J.; Zhao, G.; Terasaki, O.; Cui, C.; Yang, J.; Liu, C.; et al. Synthesis of Amino Acids by Electrocatalytic Reduction of CO2 on Chiral Cu Surfaces. *Chem* **2023**, *9*, 460–471, doi:10.1016/j.chempr.2022.10.017.
173. Tan, J.; Shelton, J.L.; Wright, D.; Haque, M.A.; Saund, S.S.; Ghoshal, D.; Le, T.H.; Dong, Y.; Smeaton, M.A.; Jungjohann, K.L.; et al. Chirality Induced Spin Selectivity Suppresses Competing Hydrogen Evolution during Electrochemical CO2 Reduction 2025.
174. Pu, Y.; Wang, T.; Lin, C.; Wang, D.; Liu, Z.; Tian, Y.; Wang, J. Enhancement of Photocatalytic CO_2 Reduction in BiOBr through Chirality-Induced Electron Spin Polarization Regulation. *Chem. Commun.* **2025**, *61*, 2580–2583, doi:10.1039/D4CC06009A.
175. Moon, Y.H.; Kim, N.Y.; Kim, S.M.; Jang, Y.J. Recent Advances in Electrochemical Nitrogen Reduction Reaction to Ammonia from the Catalyst to the System. *Catalysts* **2022**, *12*, 1015, doi:10.3390/catal12091015.
176. Kiran, V.; Mathew, S.P.; Cohen, S.R.; Hernández Delgado, I.; Lacour, J.; Naaman, R. Helicenes—A New Class of Organic Spin Filter. *Adv. Mater.* **2016**, *28*, 1957–1962, doi:10.1002/adma.201504725.
177. Fu, X.; Zhang, J.; Kang, Y. Recent Advances and Challenges of Electrochemical Ammonia Synthesis. *Chem Catal.* **2022**, *2*, 2590–2613, doi:10.1016/j.checat.2022.09.001.
178. Fernández, C.A.; Chapman, O.; Brown, M.A.; Alvarez-Pugliese, C.E.; Hatzell, M.C. Achieving Decentralized, Electrified, and Decarbonized Ammonia Production. *Environ. Sci. Technol.* **2024**, *58*, 6964–6977, doi:10.1021/acs.est.3c10751.
179. Li, W.; Li, K.; Ye, Y.; Zhang, S.; Liu, Y.; Wang, G.; Liang, C.; Zhang, H.; Zhao, H. Efficient Electrocatalytic Nitrogen Reduction to Ammonia with Aqueous Silver Nanodots. *Commun. Chem.* **2021**, *4*, 10, doi:10.1038/s42004-021-00449-7.
180. Guo, C.; Yang, S.; Wei, L.; Su, J.; Guo, L. Enhanced Electrocatalytic Nitrogen Reduction on a Three-Dimensional Cu_3 P/SnP@CF Catalyst through a Multi-Site Synergistic Effect between the Heterointerface and Phosphorus Vacancies. *J. Mater. Chem. A* **2025**, *13*, 3634–3644, doi:10.1039/D4TA07445A.
181. Zhu, H.; Ren, X.; Yang, X.; Liang, X.; Liu, A.; Wu, G. Fe-based Catalysts for Nitrogen Reduction toward Ammonia Electrosynthesis under Ambient Conditions. *SusMat* **2022**, *2*, 214–242, doi:10.1002/sus2.70.

 doi:10.20944/preprints202603.2520.v1

182. An, T.-Y.; Surendran, S.; Jesudass, S.C.; Lee, H.; Moon, D.J.; Kim, J.K.; Sim, U. Promoting Electrochemical Ammonia Synthesis by Synergized Performances of Mo2C-Mo2N Heterostructure. *Front. Chem.* **2023**, *11*, 1122150, doi:10.3389/fchem.2023.1122150.
183. Chakraborty, D.; Petersen, H.N.; Elkjær, C.; Cagulada, A.; Johannessen, T. Solid Ammonia as Energy Carrier: Current Status and Future Prospects. *Fuel Cells Bull.* **2009**, *2009*, 12–15, doi:10.1016/S1464-2859(09)70336-0.
184. Wang, M.; Khan, M.A.; Mohsin, I.; Wicks, J.; Ip, A.H.; Sumon, K.Z.; Dinh, C.-T.; Sargent, E.H.; Gates, I.D.; Kibria, M.G. Can Sustainable Ammonia Synthesis Pathways Compete with Fossil-Fuel Based Haber–Bosch Processes? *Energy Environ. Sci.* **2021**, *14*, 2535–2548, doi:10.1039/D0EE03808C.
185. Wu, W.; Pan, J.; Wang, H.; Fan, J.; Yang, J.; Liu, Y.; Zhan, Y.; Yan, X. A High-Rate and Ultrastable Ammonium Ion-Air Battery Enabled by the Synergy of ORR and NH_4^+ Storage. *Adv. Mater.* **2025**, *37*, 2415476, doi:10.1002/adma.202415476.
186. Zheng, R.; Li, Y.; Yu, H.; Zhang, X.; Yang, D.; Yan, L.; Li, Y.; Shu, J.; Su, B. Ammonium Ion Batteries: Material, Electrochemistry and Strategy. *Angew. Chem. Int. Ed.* **2023**, *62*, e202301629, doi:10.1002/anie.202301629.
187. Jiang, H.; Chen, G.; Savateev, O.; Xue, J.; Ding, L.; Liang, Z.; Antonietti, M.; Wang, H. Enabled Efficient Ammonia Synthesis and Energy Supply in a Zinc–Nitrate Battery System by Separating Nitrate Reduction Process into Two Stages. *Angew. Chem. Int. Ed.* **2023**, *62*, e202218717, doi:10.1002/anie.202218717.
188. Jesudass, S.C.; Surendran, S.; Kim, J.Y.; An, T.-Y.; Janani, G.; Kim, T.-H.; Kim, J.K.; Sim, U. Pathways of the Electrochemical Nitrogen Reduction Reaction: From Ammonia Synthesis to Metal-N2 Batteries. *Electrochem. Energy Rev.* **2023**, *6*, 27, doi:10.1007/s41918-023-00186-6.
189. Ma, J.-L.; Bao, D.; Shi, M.-M.; Yan, J.-M.; Zhang, X.-B. Reversible Nitrogen Fixation Based on a Rechargeable Lithium-Nitrogen Battery for Energy Storage. *Chem* **2017**, *2*, 525–532, doi:10.1016/j.chempr.2017.03.016.
190. Guo, Y.; Yang, Q.; Wang, D.; Li, H.; Huang, Z.; Li, X.; Zhao, Y.; Dong, B.; Zhi, C. A Rechargeable Al–N_2 Battery for Energy Storage and Highly Efficient N_2 Fixation. *Energy Environ. Sci.* **2020**, *13*, 2888–2895, doi:10.1039/D0EE01241F.
191. Ren, J.-T.; Chen, L.; Liu, Y.; Yuan, Z.-Y. Hollow Cobalt Phosphate Microspheres for Sustainable Electrochemical Ammonia Production through Rechargeable Zn–N_2 Batteries. *J. Mater. Chem. A* **2021**, *9*, 11370–11380, doi:10.1039/D1TA01144H.
192. Du, C.; Gao, Y.; Wang, J.; Chen, W. Achieving 59% Faradaic Efficiency of the N_2 Electroreduction Reaction in an Aqueous Zn–N_2 Battery by Facilely Regulating the Surface Mass Transport on Metallic Copper. *Chem. Commun.* **2019**, *55*, 12801–12804, doi:10.1039/C9CC05978D.
193. Ge, B.; Wang, Y.; Sun, Y.; Li, Y.; Huang, J.; Peng, Q. A Proof-of-Concept of Na-N2 Rechargeable Battery. *Energy Storage Mater.* **2019**, *23*, 733–740, doi:10.1016/j.ensm.2019.02.018.
194. Gupta, R.; Balo, A.; Garg, R.; Mondal, A.K.; Ghosh, K.B.; Chandra Mondal, P. The Chirality-Induced Spin Selectivity Effect in Asymmetric Spin Transport: From Solution to Device Applications. *Chem. Sci.* **2024**, *15*, 18751–18771, doi:10.1039/D4SC05736H.
195. Kulkarni, C.; Mondal, A.K.; Das, T.K.; Grinbom, G.; Tassinari, F.; Mabesoone, M.F.J.; Meijer, E.W.; Naaman, R. Highly Efficient and Tunable Filtering of Electrons' Spin by Supramolecular Chirality of Nanofiber-Based Materials. *Adv. Mater.* **2020**, *32*, 1904965, doi:10.1002/adma.201904965.
196. Islam, J.; Shareef, M.; Zabed, H.M.; Qi, X.; Chowdhury, F.I.; Das, J.; Uddin, J.; Kaneti, Y.V.; Khandaker, M.U.; Ullah, Md.H.; et al. Electrochemical Nitrogen Fixation in Metal-N2 Batteries: A Paradigm for Simultaneous NH3 Synthesis and Energy Generation. *Energy Storage Mater.* **2023**, *54*, 98–119, doi:10.1016/j.ensm.2022.10.007.
197. Ren, J.-T.; Chen, L.; Wang, H.-Y.; Yuan, Z.-Y. Aqueous Al-N2 Battery Assembled by Hollow Molybdenum Phosphate Microspheres for Simultaneous NH3 Production and Power Generation. *Chem. Eng. J.* **2021**, *418*, 129447, doi:10.1016/j.cej.2021.129447.
198. Ren, J.-T.; Chen, L.; Wang, H.-Y.; Yuan, Z.-Y. Aqueous Rechargeable Zn–N_2 Battery Assembled by Bifunctional Cobalt Phosphate Nanocrystals-Loaded Carbon Nanosheets for Simultaneous NH_3 Production and Power Generation. *ACS Appl. Mater. Interfaces* **2021**, *13*, 12106–12117, doi:10.1021/acsami.1c00570.

 doi:10.20944/preprints202603.2520.v1

199. Wang, H.; Si, J.; Zhang, T.; Li, Y.; Yang, B.; Li, Z.; Chen, J.; Wen, Z.; Yuan, C.; Lei, L.; et al. Exfoliated Metallic Niobium Disulfate Nanosheets for Enhanced Electrochemical Ammonia Synthesis and Zn-N2 Battery. *Appl. Catal. B Environ.* **2020**, *270*, 118892, doi:10.1016/j.apcatb.2020.118892.
200. Lv, X.-W.; Liu, X.-L.; Gao, L.-J.; Liu, Y.-P.; Yuan, Z.-Y. Iron-Doped Titanium Dioxide Hollow Nanospheres for Efficient Nitrogen Fixation and Zn–N_2 Aqueous Batteries. *J. Mater. Chem. A* **2021**, *9*, 4026–4035, doi:10.1039/D0TA11244E.
201. Wang, H.; Li, Z.; Li, Y.; Yang, B.; Chen, J.; Lei, L.; Wang, S.; Hou, Y. An Exfoliated Iron Phosphorus Trisulfide Nanosheet with Rich Sulfur Vacancy for Efficient Dinitrogen Fixation and Zn-N2 Battery. *Nano Energy* **2021**, *81*, 105613, doi:10.1016/j.nanoen.2020.105613.
202. Lv, X.-W.; Liu, Y.; Wang, Y.-S.; Liu, X.-L.; Yuan, Z.-Y. Encapsulating Vanadium Nitride Nanodots into N,S-Codoped Graphitized Carbon for Synergistic Electrocatalytic Nitrogen Reduction and Aqueous Zn-N2 Battery. *Appl. Catal. B Environ.* **2021**, *280*, 119434, doi:10.1016/j.apcatb.2020.119434.
203. Jérome, D.; Schulz, H.J. Organic Conductors and Superconductors. *Adv. Phys.* **1982**, *31*, 299–490, doi:10.1080/00018738200101398.
204. Vieri, H.M.; Kim, M.-C.; Badakhsh, A.; Choi, S.H. Electrochemical Synthesis of Ammonia via Nitrogen Reduction and Oxygen Evolution Reactions—A Comprehensive Review on Electrolyte-Supported Cells. *Energies* **2024**, *17*, 441, doi:10.3390/en17020441.
205. Mu, J.; Gao, X.; Yu, T.; Zhao, L.; Luo, W.; Yang, H.; Liu, Z.; Sun, Z.; Gu, Q.; Li, F. Ambient Electrochemical Ammonia Synthesis: From Theoretical Guidance to Catalyst Design. *Adv. Sci.* **2024**, *11*, 2308979, doi:10.1002/advs.202308979.
206. Singh, A.N.; Anand, R.; Zafari, M.; Ha, M.; Kim, K.S. Progress in Single/Multi Atoms and 2D-Nanomaterials for Electro/Photocatalytic Nitrogen Reduction: Experimental, Computational and Machine Leaning Developments. *Adv. Energy Mater.* **2024**, *14*, 2304106, doi:10.1002/aenm.202304106.
207. Ling, C.; Bai, X.; Ouyang, Y.; Du, A.; Wang, J. Single Molybdenum Atom Anchored on N-Doped Carbon as a Promising Electrocatalyst for Nitrogen Reduction into Ammonia at Ambient Conditions. *J. Phys. Chem. C* **2018**, *122*, 16842–16847, doi:10.1021/acs.jpcc.8b05257.
208. Zhong, W.; Gong, Z.; Chen, P.; Cao, Q.; Liu, X.; Chen, Y.; Lin, Z. Electrochemical Reduction of Nitrate to Ammonia: From Fundamental Understanding to Practical Applications. *Chem Catal.* **2024**, *4*, 101060, doi:10.1016/j.checat.2024.101060.
209. Lee, H.K.; Koh, C.S.L.; Lee, Y.H.; Liu, C.; Phang, I.Y.; Han, X.; Tsung, C.-K.; Ling, X.Y. Favoring the Unfavored: Selective Electrochemical Nitrogen Fixation Using a Reticular Chemistry Approach. *Sci. Adv.* **2018**, *4*, eaar3208, doi:10.1126/sciadv.aar3208.
210. Yuan, S.; Meng, G.; Liu, D.; Zhao, W.; Zhu, H.; Chi, Y.; Ren, H.; Guo, W. Synergy of Substrate Chemical Environments and Single-Atom Catalysts Promotes Catalytic Performance: Nitrogen Reduction on Chiral and Defected Carbon Nanotubes. *ACS Appl. Mater. Interfaces* **2022**, *14*, 52544–52552, doi:10.1021/acsami.2c17280.
211. Zheng, S.-J.; Chen, H.; Zang, S.-Q.; Cai, J. Chiral-Induced Spin Selectivity in Electrocatalysis. *Matter* **2025**, *8*, 101924, doi:10.1016/j.matt.2024.11.018.
212. Nakajima, R.; Hirobe, D.; Kawaguchi, G.; Nabei, Y.; Sato, T.; Narushima, T.; Okamoto, H.; Yamamoto, H.M. Giant Spin Polarization and a Pair of Antiparallel Spins in a Chiral Superconductor. *Nature* **2023**, *613*, 479–484, doi:10.1038/s41586-022-05589-x.